115

Tangential stress beneath wind-driven air–water interfaces

By MICHAEL L. BANNER AND WILLIAM L. PEIRSON

School of Mathematics, The University of New South Wales, Sydney, Australia
e-mail: M.Banner@unsw.edu.au

The detailed structure of the aqueous surface sublayer flow immediately adjacent to the wind-driven air–water interface is investigated in a laboratory wind-wave flume using particle image velocimetry (PIV) techniques. The goal is to investigate quantitatively the character of the flow in this crucial, very thin region which is often disrupted by microscale breaking events. In this study, we also examine critically the conclusions of Okuda, Kawai & Toba (1977), who argued that for very short, strongly forced wind-wave conditions, shear stress is the dominant mechanism for transmitting the atmospheric wind stress into the water motion – waves and surface drift currents. In strong contrast, other authors have more recently observed very substantial normal stress contributions on the air side. The availability of PIV and associated image technology now permits a timely re-examination of the results of Okuda *et al.*, which have been influential in shaping present perceptions of the physics of this dynamically important region. The PIV technique used in the present study overcomes many of the inherent shortcomings of the hydrogen bubble measurements, and allows reliable determination of the fluid velocity and shear within 200 μm of the instantaneous wind-driven air–water interface.

The results obtained in this study are not in accord with the conclusions of Okuda *et al.* that the tangential stress component dominates the wind stress. It is found that prior to the formation of wind waves, the tangential stress contributes the entire wind stress, as expected. With increasing distance downwind, the mean tangential stress level decreases marginally, but as the wave field develops, the total wind stress increases significantly. Thus, the wave form drag, represented by the difference between the total wind stress and the mean tangential stress, also increases systematically with wave development and provides the major proportion of the wind stress once the waves have developed beyond their early growth stage. This scenario reconciles the question of relative importance of normal and tangential stresses at an air–water interface. Finally, consideration is given to the extrapolation of these detailed laboratory results to the field, where the present findings suggest that the sea surface is unlikely to become fully aerodynamically rough, at least for moderate to strong winds.

1. Introduction

Close-range observation of the wind-driven sea surface for conditions ranging over light to strong winds reveals a microstructure made up of small-scale breaking waves, commonly referred to as microscale breakers. A typical example is shown in figure 1, which was photographed at a mean elevation of 6 m above the mean water level from an oil platform in Bass Strait during a steady 12 m s^{-1} wind. The very short waves highlighted by their bright crest lines in this 4 m × 2.6 m sea surface image have
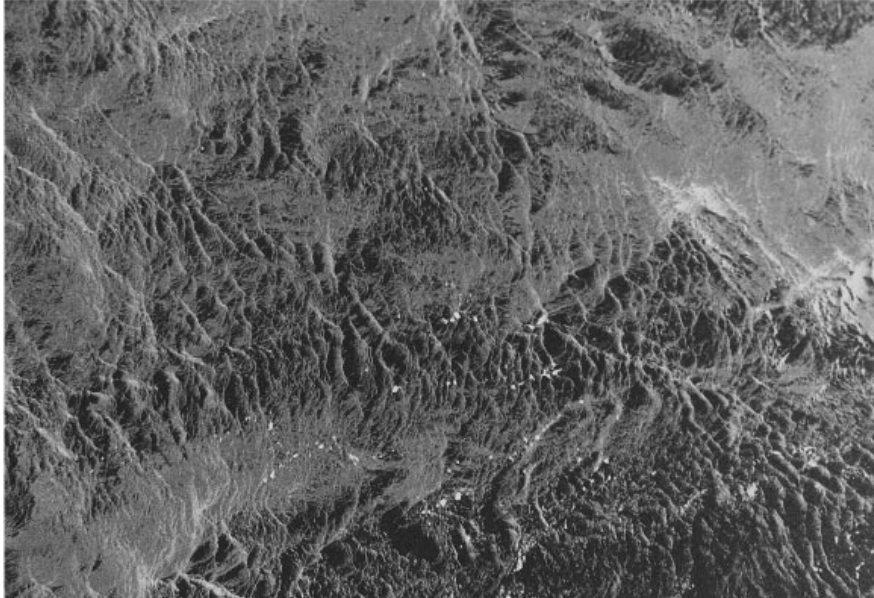
FIGURE 1. A close range photograph from 6 m above the sea surface showing its fine structure for open ocean wave conditions of 3 m significant wave height with a wind speed of 12 m s⁻¹ from the top right to the lower left. The field of view is 4 m × 2.6 m, indicating microscale breakers with 50 mm to 150 mm wavelengths.

wavelengths of several centimetres, are very strongly forced by the overlying surface wind and, as a consequence, are frequently in a state of microscale breaking, i.e. breaking without air entrainment. Fundamental questions associated with these structures concern the existence of viscous sublayers under such conditions, as well as the relative strength of the associated tangential stress in the concomitant air–sea momentum exchange process. Owing to the profound difficulties in conducting *in situ* measurements, one is forced to retreat to the laboratory to gain insight into such issues through carefully executed wind-wave tank experiments. Even here, the task is daunting: typical interfacial microscale breaking wave structures still dominate the interface once the waves have arisen, as is evident in the typical interfacial structures seen in figure 2. Probing the thin interfacial aqueous layer within 1 mm of the highly unsteady interface for velocity and shear information clearly constitutes a significant observational challenge. Before describing how modern particle imaging technology and techniques have allowed remarkable progress with such measurements, we present a brief review of the scientific background of this problem.

There is a long history of observational and theoretical research on improving our understanding of the physics of the momentum exchange between wind and the underlying water surface. The critical discussion by Donelan (1990, §§2–4) provides a comprehensive reference source for the background to this subject and highlights the associated contemporary issues. A major difficulty has been the lack of detailed information on the character of the airflow over real wind-driven, wavy water surfaces with due regard to the presence of breaking waves, including microscale breakers as well as whitecaps. Notable progress in this context was made some twenty years ago with the results of Banner & Melville (1976), who reported laboratory observations of air flow separation over breaking wave crests. They concluded that flow separation and a significant level of local wind stress enhancement was directly associated with wave
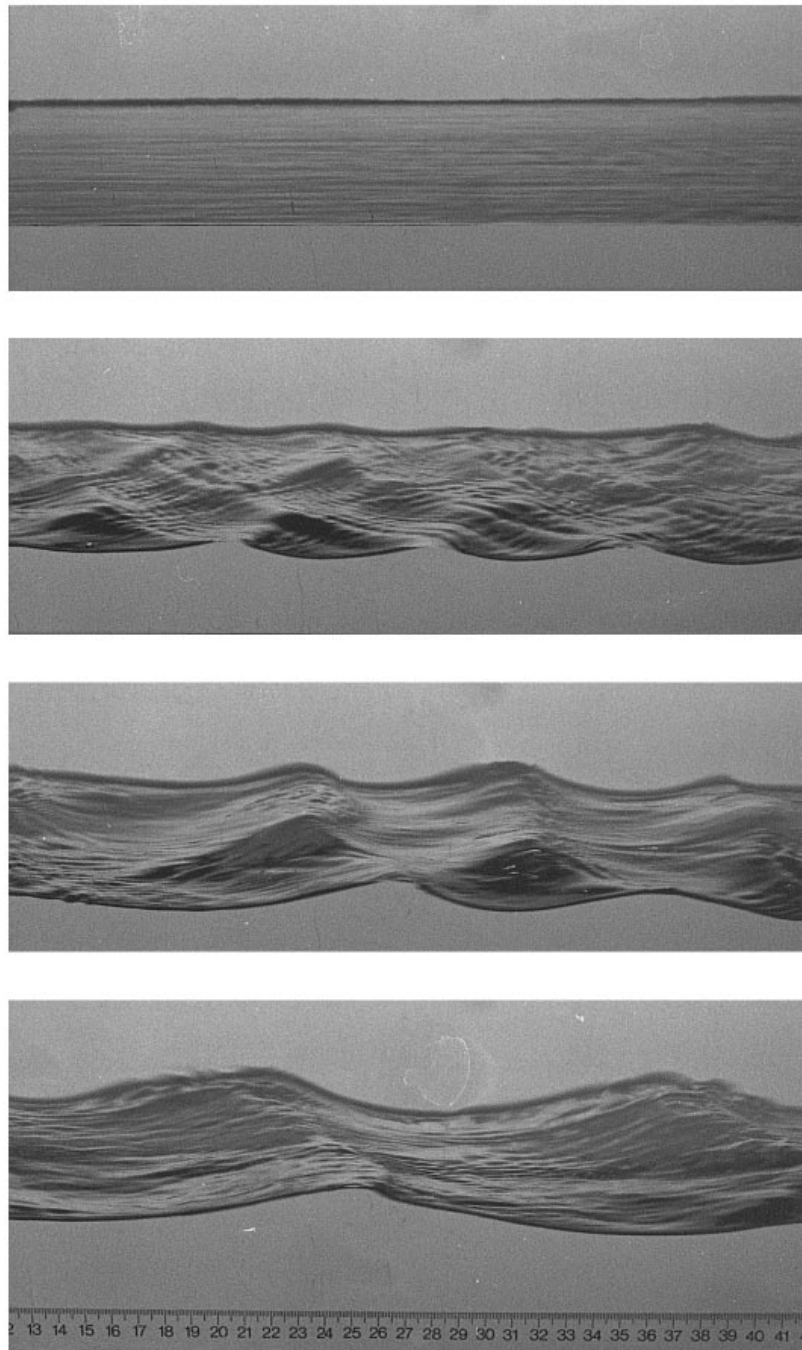
FIGURE 2. Photographs of wave conditions within the laboratory flume. The wind and waves are moving from left to right. From the upper to lower panel: wind speed 8.1 m s^{-1}, fetch 0.13 m; wind speed 4.8 m s^{-1}, fetch 4.35 m; wind speed 6.3 m s^{-1}, fetch 4.35 m; wind speed 8.1 m s^{-1}, fetch 4.35 m.

breaking. This work indicated that wave form drag (paralleling the 'sheltering hypothesis' of Jeffreys (1924, 1925)) was a potentially significant contributor to the momentum flux between the atmosphere and the surface wave field. Around the same time, Okuda *et al.* (1977; hereinafter referred to as O77), published a detailed laboratory study that examined the structure of the aqueous boundary layer at the air–sea interface. This study was directed at quantifying the importance of tangential stress at the interface by estimating the near surface shear in the water, deduced from flow-visualization data obtained from hydrogen bubble lines created by a surface-piercing wire. O77 concluded that for strongly wind-forced wavelets at relatively short fetches (2.85 m), the wind stress was predominantly supported by the skin friction or equivalently, tangential stress, and, therefore, that the contribution of wave form drag (or normal stress) was limited to only a few per cent of the total wind stress. More recently, Banner (1990) reported results from a detailed study of surface pressure distributions over laboratory wind-driven, mechanically initiated waves. Measured surface pressure distributions were used to compute the form drag over wind waves. In direct contrast with the results of O77, Banner (1990) concluded that for such wind-wave conditions, the form drag provided the dominant contribution, approximately $O(0.7 \text{ to } 0.8)$, to the total wind stress.

The present study has been undertaken in an effort to reconcile the disparities between these two conflicting conclusions. In particular, the particle image velocimetry (PIV) technique has provided an opportunity to reassess the magnitude of tangential stresses near the interface. We begin by reviewing previous studies of surface tangential stresses and then describe the experimental techniques based on PIV that were used for the present investigation. A detailed comparison of our PIV results is made with previous results inferred from hydrogen bubble analyses, and conclusions are drawn on the relative importance of normal and tangential stress contributions to the overall interfacial wind stress for short fetches. The paper concludes with a discussion of the implications of these findings for open ocean conditions.

2. Previous studies

Whilst many studies have examined surface-wind-driven velocities with relatively large (> 1 mm) tracers, few investigators have attempted experiments with particle tracers of sufficiently small scale to measure reliably the near-surface shear in the aqueous viscous sublayer.

The earliest experimental studies of surface shear were initiated by McLeish & Putland (1975). These were not intended to be comprehensive but to support conclusions about surface heat transfer. Hydrogen bubbles were used in a laboratory flume to visualize flow within the near-surface layer, whose motion was captured by photographs of 62.5 ms exposure. At very short (unspecified) fetch prior to the onset of wind waves, the tangential stress was reported to be 0.1 and 0.2 Pa for wind speeds of 5.5 and 9.0 m s^{-1}, respectively. Further downwind, in a region of initial wind-wave development, they reported a reduction in the indicated tangential stress (0.07 Pa) for a 5.5 m s^{-1} wind.

A second, and far more detailed, study was undertaken shortly afterwards by O77. This was conducted in a wind-wave tunnel 150 mm wide $\times$ 4.55 m long with an air channel 170 mm high and a water depth of 530 mm. Observations were made of wind waves generated at a fetch of 2.85 m with a mean wind speed of 6.2 m s^{-1}. The characteristic wave period, length and height of the generated wavelets at this fetch were 0.23 s, 83 mm and 9.4 mm, respectively. Hydrogen bubbles were used to visualize

and quantify the flow field. These were generated using a 50 μm diameter platinum wire and generated every 40 ms with a pulse of 2 ms duration. The bubbles were illuminated by a stroboscope and the images captured by a ciné camera with 24 ms between exposures. The authors made a number of significant improvements in their technique over that used by McLeish & Putland (1975). In particular, the size of the generated bubbles was recorded, the rise velocities were inferred and corrections were made to the bubble trajectories for the buoyant rise of the bubbles. The near-surface shear layer along the wave profile was assessed in terms of its magnitude and the thickness of the viscous layer. The presence of strong tangential stress was indicated on the upwind face of the waves, increasing in intensity towards the crest. On the lee face of the waves, the tangential stress was assessed as negligible. The stress supported by the tangential shear was estimated to be between 0.36 Pa and 0.40 Pa. These stresses were shown to increase from about 0.1 Pa in the trough to a value of between 1.2 and 1.6 Pa just upwind of the crest. The total stress computed from the mean wind profile was given as 0.30 Pa. It was therefore concluded by O77 that the normal stress was negligible and the tangential stress dominated the interfacial wind stress. The phasing of their tangential stress distribution over the wave profile also implied a dominant contribution of the tangential stress to the wave-coherent wind stress.

These results had led other authors to speculate on the dominant role of shear stress contributions (e.g. Csanady (1985, 1990), amongst others) in air–sea momentum exchange. However, there are potentially serious problems associated with the underlying supportive data provided by O77. In particular, there are a number of difficulties that arise with the quantitative use of hydrogen bubble measurements near a rapidly oscillating free surface that were not addressed by O77. These are:

(i) The assumption that the presence of a hydrogen wire of 50 μm diameter had no influence on the velocity distribution downstream. Wilkinson & Willoughby (1981) showed that the influence of a velocity deficit created by a wire wake on hydrogen bubbles can extend up to 500 diameters downstream, in this case a distance of 25 mm. This is the size of the entire field of view used by O77. Therefore, without careful and detailed investigation, analyses of bubble behaviour in a region of high shear must involve some uncertainty due to wire wake effects.

(ii) The tracers used were inappropriately large. Within O77, it is claimed that shear is being measured in a region between 100 and 600 μm thick. However, the bubbles themselves were recorded as having diameters of between 120 and 160 μm. Within the region just upwind of the crest ($-60°$ to $0°$ phase), the linear sublayer was estimated to have a mean thickness of approximately 200 μm. It is precisely within this region that the largest tangential stress was calculated. These are fundamental to the conclusion of the dominance of skin friction over the entire waveform.

The tangential stress in the viscous sublayer was estimated from the relation $\tau_{tang} = \mu \Delta S w \cos\theta / \delta^2$, where $\Delta S \equiv (S(0) - S(-\delta)) - (S(-\delta) - S(-2\delta))$. Here τ_{tang} is the estimated tangential stress, μ is the dynamic viscosity of water, θ is the slope of the water surface, $S(z)$ is the bubble displacement at depth z, w is the bubble ascent velocity and δ is half the viscous sublayer thickness. Evaluation of ΔS involves obtaining reliable relative displacement estimates for at least three depths from the surface. This is simply not feasible when the sublayer thickness is less than twice the tracer diameter. In addition, the surface velocity $S(0)$, a critical term, cannot be reliably measured by such relatively large tracers.

(iii) No assessment was made of the influence of the free surface on the rising bubbles in the O77 methodology. Bubbles that reach the surface will immediately be impeded by surface tension and have their vertical velocity reduced substantially. Any

overestimate of bubble rise velocities will result in a corresponding overestimation of shear stress. In addition, bubbles protruding above the surface will be exposed to a drag force by the overlying wind, producing artificially high values of $S(0)$, again resulting in overestimation of the tangential stress.

(iv) The rise velocity of the tracers was relatively high. From bubble size estimates, the mean rise velocity was inferred to be 9.1 mm s^{-1}. The time between visualizations of the flow was approximately 24 ms. Over this period each bubble would be expected to rise 220 μm. This distance is equivalent to the estimated linear sublayer thickness within the critical region. The measurements are not founded on the monitoring of individual bubble motion, but are based on comparing near-surface profiles formed by bubbles leaving the wire at different depths in the flow. O77 used assumed velocity distributions to account for this effect, thereby introducing a potentially major weakness in the technique.

Consequently, it is argued that previous studies of the aqueous surface boundary layer using hydrogen bubbles may have had some serious problems with their methodology and their conclusions are open to question. The next section describes a laboratory instrumentation system designed to overcome these weaknesses.

3. Experimental configuration

The experimental facility used in this investigation is similar to that used by Banner (1990). The wind-wave tank is 220 mm wide $\times$ 8 m long, with a wind-tunnel section transitioning smoothly over the water surface. For the experiments described here, the depth of water was 200 mm with a 420 mm deep air channel above. The experiments reported here were undertaken for a range of fetches (distance from the first point of contact of the wind over the water) from 0.13 m to 4.35 m to determine the variation with wave development at a centreline wind speed $U_c = 6.3$ m s^{-1} measured at a height of 210 mm above the water surface. Supplementary measurements at higher ($U_c = 8.1$ m s^{-1}) and lower ($U_c = 4.8$ m s^{-1}) wind speeds were made to examine the wind speed dependence of the results.

The properties of the wind wavelets generated at these very short fetches vary strongly with fetch and wind speed. No waves were present at the shortest fetch (0.13 m) for each wind speed. Wavelets were present at the longer fetches and, being overdriven by the wind input, were generally in a state of microscale breaking. Relevant details of the observed wind and wave properties are summarized in table 1.

The wave properties were recorded using a high-resolution impedance wire probe digitized at a rate of 1 kHz. The local mean wavelength and mean wave slope for each wind speed and fetch were estimated from an ensemble of images of the wave profiles. The observed mean frequency f_p was determined from the spectral peak frequency determined from the wave-probe signal. However, the observed frequency of these short-fetch waves is potentially influenced by their advection by the wind drift current, together with other effects such as finite wave slope, strong amplitude and wavenumber modulation, and rotationality. In order to indicate the typical order of magnitude of these effects, we also included in table 1 a linear theory estimate of the wave frequency calculated from the observed wavelength, as it was not possible to reliably determine the intrinsic wind-wave propagation speed. In any event, the estimates of f_p are provided primarily for the purpose of relating our primary data to previous studies in which similar approximations were used to characterize their wind waves.

An effort was made to quantify the occurrence of microscale breaking by recording the percentage passage rate of breaking wavelets past the measurement site, using the

Test date	Error (±)	951124	950830	950721	950615	950614	950815	951124	951130	950831	O77
U_{cl} (m s⁻¹)	3%	4.8	4.8	6.3	6.3	6.3	6.3	8.1	8.1	8.1	6.9
Fetch (m)	<1%	0.13	4.35	0.13	2.45	3.1	4.35	0.13	2.45	4.35	2.85
Water temperature	0.5°	17	15	13	13.6	14.4	11	17	20	15	—
Mean wave height (mm)	2%	0	5.4	0	6.2	8.0	10.1	0	10.1	14.3	9.4
Wave energy (mm²)	4%	0	4.9	0	6.8	12.8	14.9	0	16.2	30.8	—
Wavelength (mm)	2%	0	78	0	78	108	127	0	121	174	83
f_p (Hz)	2%	—	5.06	—	5.37	4.86	3.86	—	4.17	3.33	—
f_p (linear theory) (Hz)	2%	—	4.47	—	4.47	3.80	3.51	—	3.59	3.00	—
Mean wave slope	1%	0	0.25	0	0.28	0.28	0.27	0	0.29	0.28	—
Breaking fraction	5%	0	0.53	0	0.87	0.94	0.70	0	0.95	0.89	—
u_* (m s⁻¹)	10%	0.18	0.26	0.26	0.32	0.35	0.37	0.31	0.40	0.46	0.50
$U_{\lambda/2}$ (m s⁻¹)	5%	0	3.6	0	5.8	6.1	5.5	0	7.3	7.9	5.9
U_{10} (m s⁻¹)	12%	6.4	7.2	9.4	10.1	10.5	10.1	11.2	11.8	12.8	12.8
τ (Pa)	20%	0.039	0.083	0.080	0.125	0.150	0.168	0.114	0.199	0.261	0.303
z_0 (mm)	50%	0.0059	0.1600	0.0044	0.0310	0.0610	0.1770	0.0044	0.0814	0.1510	0.3300
$R_t = u_* z_0/\nu_a$	60%	0.07	2.85	0.08	0.68	1.46	4.49	0.09	2.25	4.78	—
Number of PIV observations	—	20	137	20	142	124	135	29	146	135	80 (waves)
Sample mean u_s (m s⁻¹)	0.5%	0.086	0.116	0.125	0.135	0.128	0.174	0.156	0.192	0.189	—
Estimated mean u_s (m s⁻¹)	0.5%	0.086	0.081	0.125	0.089	0.091	0.117	0.156	0.118	0.130	—
Sample mean τ_{tang}	10–15%	0.039	0.072	0.082	0.116	0.105	0.112	0.116	0.158	0.135	—
Estimated mean τ_{tang} (Pa)	O(0.01)	0.039	0.052	0.082	0.074	0.073	0.074	0.116	0.088	0.082	0.36
Revised mean τ_{tang} (Pa)	O(15%)	0.039	0.051	0.082	0.075	0.073	0.071	0.116	0.086	0.084	—
$\langle \tau_{tang} u_{sw}/c \rangle$ (Pa)	5%	—	0.0005	—	0.0129	0.0172	0.0085	—	0.0109	0.0089	N/A

TABLE 1. Summary of the experimental conditions and mean results. The O77 results are shown in the last column
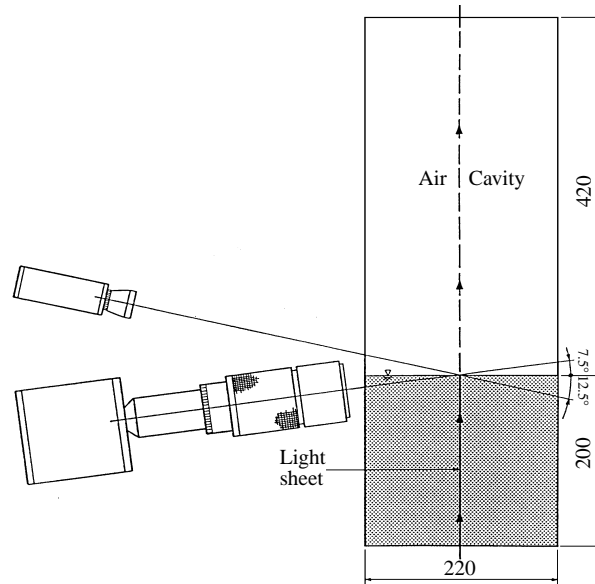
FIGURE 3. Section through wave tank showing alignment of light sheet and cameras. The PIV camera is on the lower left-hand side, looking upward. The smaller videocamera on the upper left-hand side captures the wave profile.

method proposed in Banner (1990) in which a breaking wave detection corresponds to a local slope threshold being exceeded on the leeward (downwind) face of the wave corresponding to the leading edge of the spilling breaker. A visual impression of the character of the water surface at the different fetches is given in figure 2, while details of the properties of the wind waves including their estimated breaking statistics are given in table 1. Also presented in this table are estimates of the local wind forcing of the surface. The total wind stress τ, the wind friction velocity u_*^a and the air roughness length z_0^a were determined for each experiment using the standard method of fitting to the logarithmic sublayer region of the mean velocity profile measured in the air flow with a miniature Pitot-static probe connected to a high resolution electronic manometer. To complete the specification, table 1 also shows the wind speed at a height of half the dominant water-wave length above the mean water level and provides error estimates for all observed and inferred quantities.

4. Measurement of surface tangential stress

To carry out the primary goals of this study, a specialized high-resolution particle image velocimetry (PIV) system has been developed to examine near-surface currents beneath wind-generated wavelets, with wavelets of $O(100 \text{ mm})$ that are comparable in scale to those examined by O77 and to those commonly associated with wind gusting over the ocean, as evident in figure 1. A summary of the system characteristics and capability is contained here. For more information, the reader is referred to the detailed description in Peirson (1997). Figure 3 shows the general physical arrangement of the components, for which a detailed description follows.

A 6 W water-cooled argon ion laser with its beam directed at a rotating wheel with high-quality optical mirrors mounted on its periphery has been used as a pulsed light-sheet generator. A pulsed light sheet about 1 mm thick × 80 mm wide was formed along the flume centreline with a pulse period of approximately 2 ns. The water in the
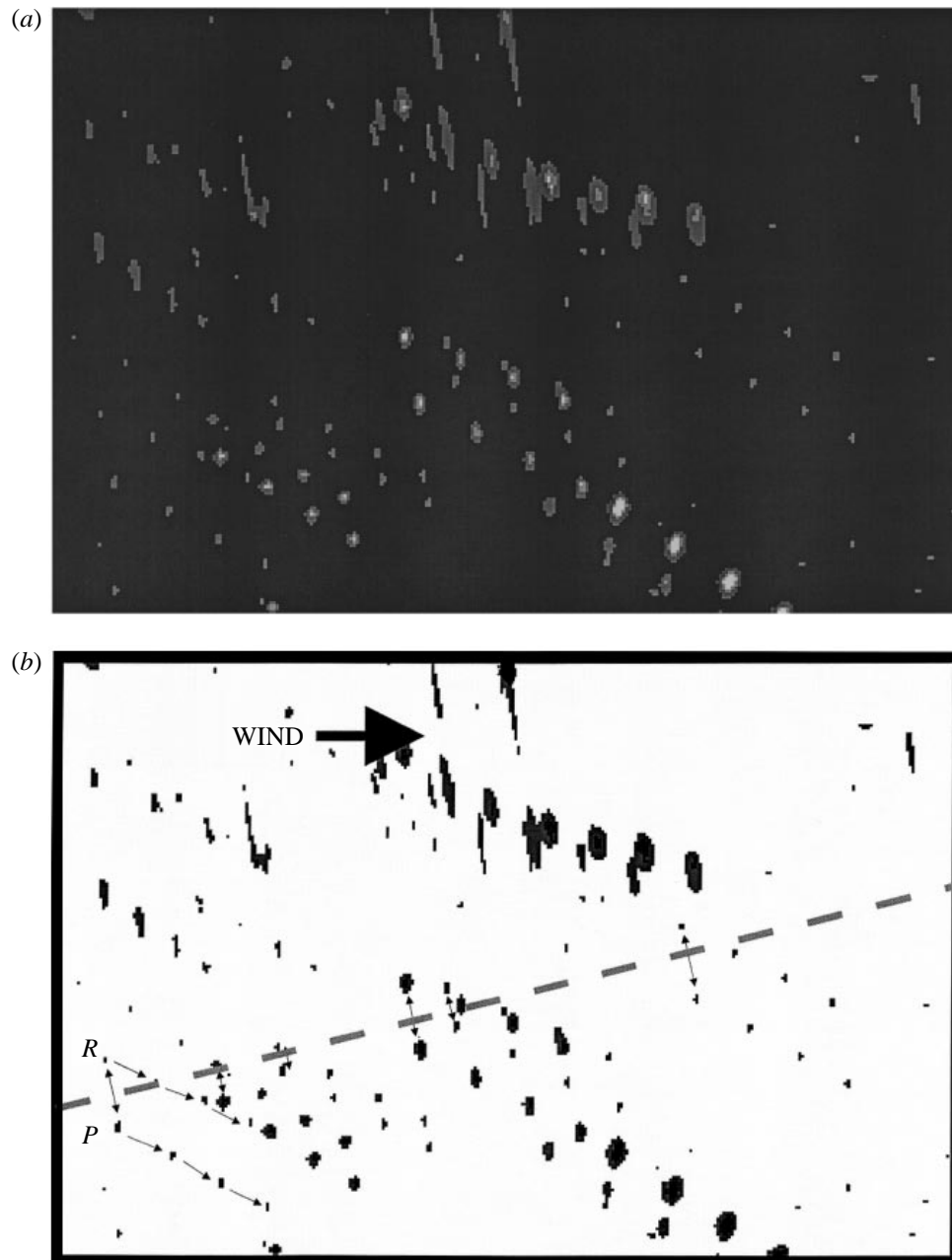
(*a*)

(*b*)

FIGURE 4. (*a*) Image segment (3.75 mm × 2.5 mm) showing particles and their reflections. (*b*) The reverse image. The approximate position of the interface is identified by the light dashed line. The leftmost particle/image pair has the subsurface particle labelled *P* and the reflection labelled *R*. Particle motion is indicated by the single-headed arrows. Other particle/image pairs resulting from the first laser pulse are indicated by double-headed arrows.

wave tank was filtered to maximize its clarity and seeded to allow the fluid motion to be visualized. The tracers used were fluorescent particles with diameters between 20 and 60 µm and a relative density of 1.2. With these particles, we experienced no difficulty in seeding the linear sublayer region. Also, the estimated position error over the pulse period owing to the density difference was below our measurement resolution.

A Kodak Megaplus CCD camera with an effective resolution of 1280 (horizontal) × 1028 (vertical) pixels was used to capture images of velocity fields below the water surface. The camera was fitted with a telephoto zoom lens (focal length 80 mm to 200 mm) and an extension bellows so that a region approximately 15 mm × 10 mm on the flume centreline could be imaged. The CCD camera has attendant hardware to enable single images to be downloaded rapidly to a controlling computer. This camera was mounted looking slightly upward at 7.5° to allow a clear view of the subsurface interface.

The laser light sheet created a well-defined line in the water surface when viewed from above. This optical property of the interface was used to provide measurements of the water surface profile and hence the phase location for the subsurface images. This was achieved with a second CCD camera, fitted with a 25 mm focal length lens, mounted rigidly above the first and viewing the surface at 12.5° from above. A second frame-grabbing card mounted in the microcomputer bus was used to capture these images. Considerable software development and careful testing were required to align the two camera images in both time and space. This was achieved using signals obtained from the light-sheet generator. Figure 3 shows the alignment of the two video cameras relative to the wave tank and the light sheet.

A system was developed to measure velocities within 1 mm of the local interface. Software was developed to enable direct displacement measurements to be made on the captured particle images at the camera resolution. As noted by O77, relatively clear reflections of subsurface particles can be observed under the relatively smooth rear face of the wave. Figure 4(*a*) shows an enlarged segment of a subsurface image. Within figure 4(*b*), particles at varying distances from the surface are identified by their multiple point images and subsurface reflections (produced by the multiple pulsing of the laser beam). Calculations have shown that for small angles of view, the position of the interface can be located reliably as being at the mid-point between a particle and its reflection. Given the laser pulsing frequency, both the velocity and location of individual particles could then be determined. Peirson (1977) provides further details of the locational aspects of the observations, concluding that all our data fell within $y^+ < 7$ of the interface, where $y^+ = yu_*/\nu$ is the standard wall coordinate used in turbulent boundary layers. This is well within the accepted viscous sublayer region.

By differencing the velocities and depths of the two centre images of each of the two proximate particles, the shear stress was determined by division of velocity difference by vertical particle separation, that is, $\tau_{tang} = \mu \Delta u / \Delta n$, where n is the local normal coordinate. In addition, the local surface velocity was derived by extrapolating to the water surface an assumed linear velocity distribution through the data points.

The present PIV methodology relies on determining differences in particle positions to obtain velocities and then differencing velocities at proximate positions to obtain velocity gradients. The resolution uncertainty for a position determination was set by the pixel size at ± 6 µm. Thus, a typical particle displacement of 0.25 mm has an uncertainty of $\pm 2\%$. With the timing between particle exposures resolved to better than $\pm 2\%$, the local velocity is determined to within better than $\pm 4\%$. For velocity gradient determination, the error increases as the distance between particles decreases. Consequently, shear stress estimates were not made if the separation of the particles

normal to the air–water interface was less than 50 μm. For typical observed vertical separations and velocity differences, the maximum uncertainty error in a local shear stress measurement was estimated at ± 0.1 Pa.

In each of our experiments, we used an ensemble of around 140 points comprised of pairs of particle images, retaining all such observations as valid data. We assessed the operational accuracy of our methodology as follows. Our 'standard' technique of analysing the two centre images of each of the two proximate particles was applied to small-slope, paddle-generated waves with no wind forcing, for which negligible shear stress was expected and a total of 60 measurements of near-surface shear stress were made. From these observations, a mean tangential stress of 0.001 Pa was obtained with an r.m.s. variability of ± 0.03 Pa. Increasing the sample size from 30 to 60 points did not change this result significantly, so this level reflects the intrinsic statistical uncertainty of our standard technique in a test-case flow with negligible shear and local unsteadiness. The time base of the measurement could be extended from 2 ms to 6 ms by differencing the velocities and depths of the two end images of each of the two proximate particles rather than the two centre images. This has the potential to reduce the uncertainties in both time and space determinations. For the paddle waves, this produced the same mean tangential stress and reduced the r.m.s. scatter by about a half. For the actual data analysis task for the strongly wind-forced wavelets shown in figure 2, we examined whether these measurement uncertainties for the different time bases would be significant compared with the natural variability in the local tangential stress at a given location on the wave profile under wind forcing. We used our standard technique for a typical mean tangential stress determination for a given phase bin, with nine individual measurements in the ensemble. The mean value was 0.100 Pa with an r.m.s. variability of ± 0.06 Pa. Analysing the outer two image points for each of the pairs of particles gave the almost identical mean value of 0.104 Pa with the r.m.s. variability reducing to ± 0.045 Pa. By comparison with the wind-free case, it is evident that significant intrinsic variability exists in the local tangential stress on wind-driven wavelets, and this exceeds the measurement uncertainty for either time base. While there was a marginal improvement in the statistical uncertainty in the tangential stress estimates at a given phase point along the wave profile, the mean level was not changed. Also, a number of individual particle image tracks clearly indicated divergence of trajectories, despite the proximity of the particles, as well as local accelerations and decelerations. Therefore observing the centre images resulted in improved localization and also in improved efficiency in cursor location when determining the particle image coordinates, especially as the last image was less intense than the others and sometimes more difficult to observe. For these reasons, we decided to proceed with our standard technique using a time base of 2 ms.

Finally, our results reveal significant scatter in the tangential stress observations which were gathered within $y^+ < 7$ in the linear sublayer. This variability is consistent with the findings of Kline *et al.* (1967) who investigated the viscous sublayer structure in turbulent boundary layers over flat plates. Their figures 10(*a*) and 10(*b*) obtained at $y^+ = 2.7$ and 4.5 established that the linear sublayer is not a laminar sublayer, but a region in which sporadic instabilities eject turbulent bursts into the outer part of the surface boundary layer. To quote directly from their paper, 'while the flow may indeed be laminar-like in this (the linear sublayer) region, it is both three-dimensional and unsteady.'
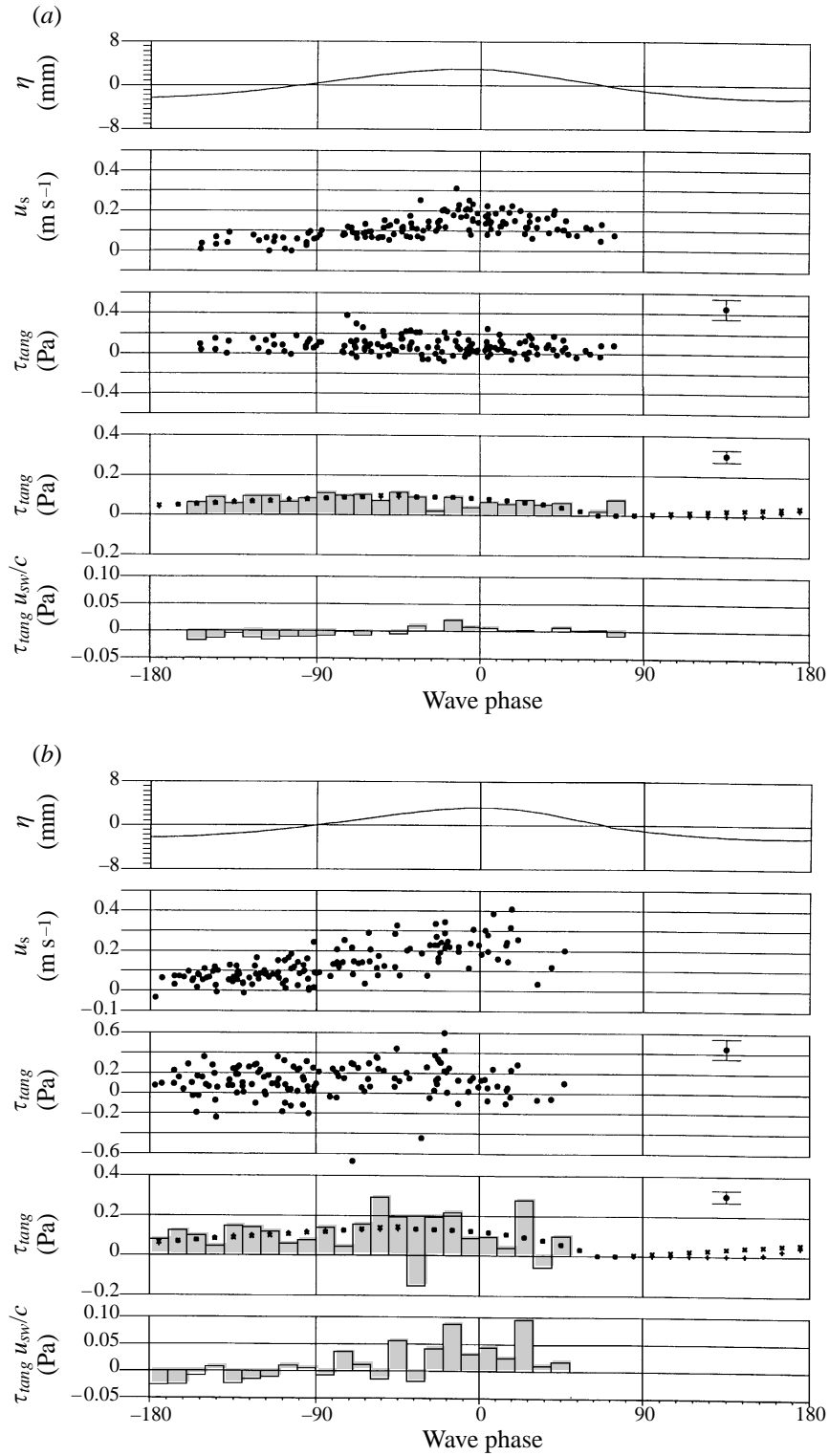
(*a*)

(*b*)

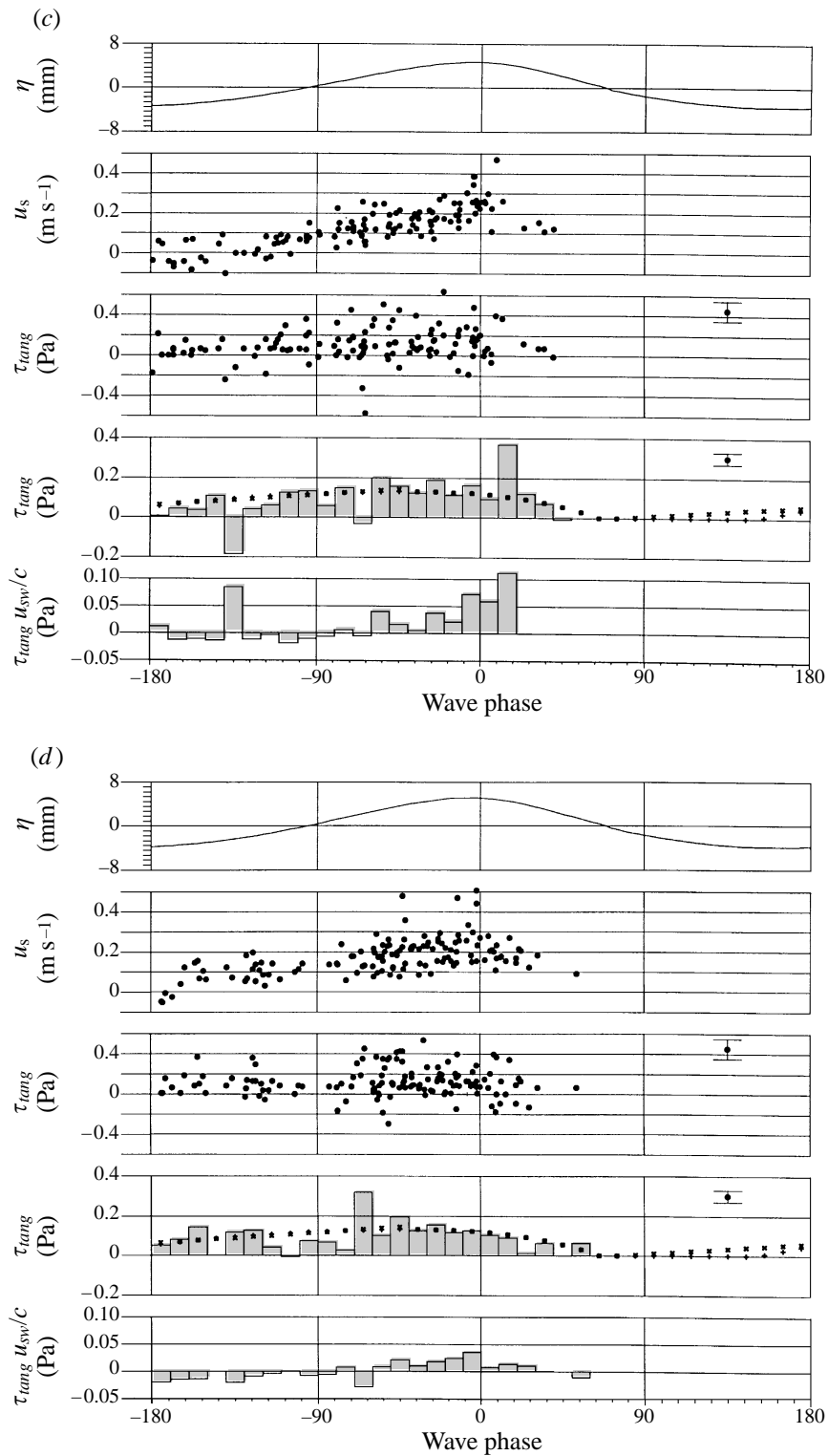FIGURE 5(*a*, *b*). For caption see page 129.

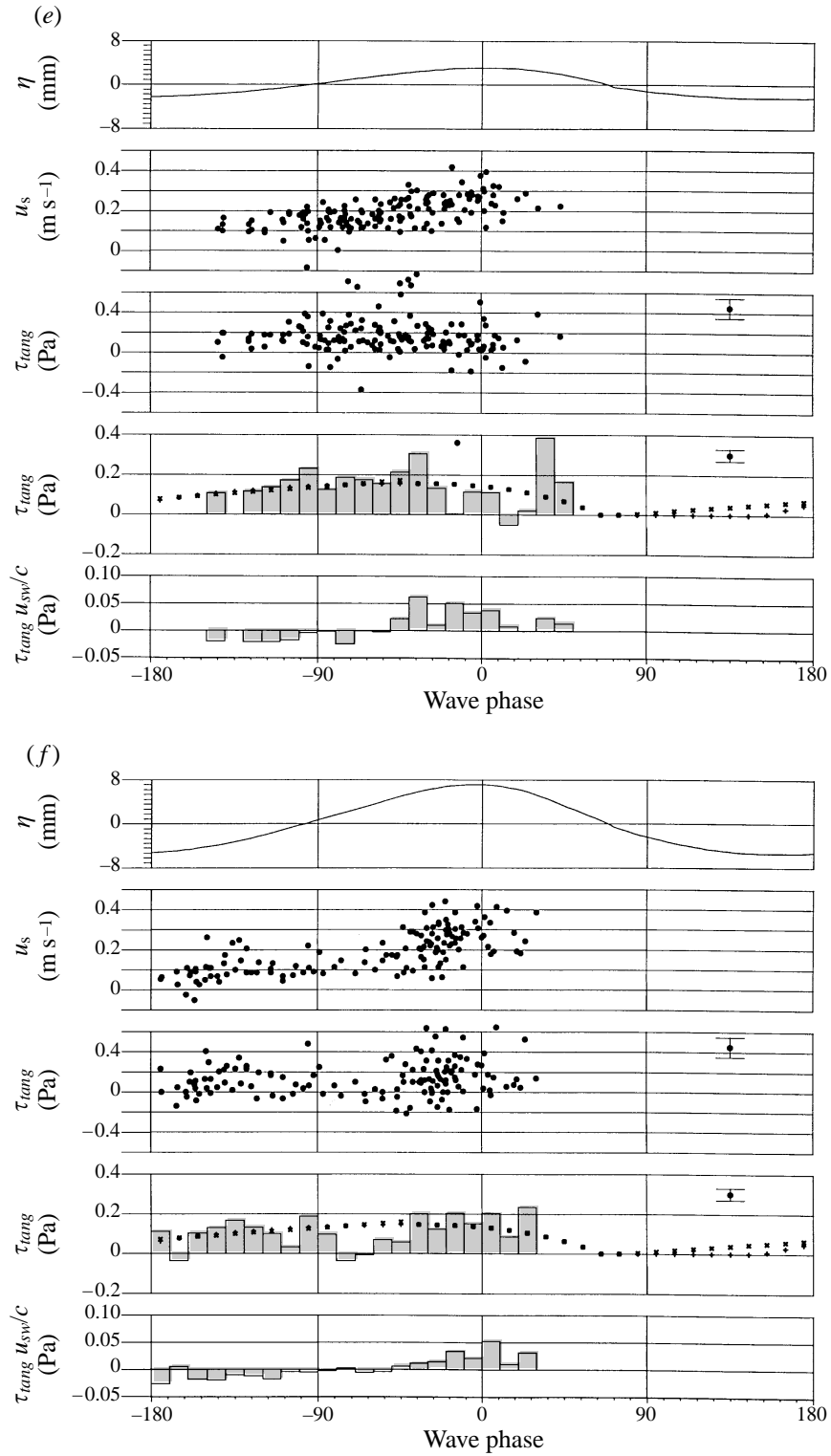FIGURE 5(*c*, *d*). For caption see page 129.
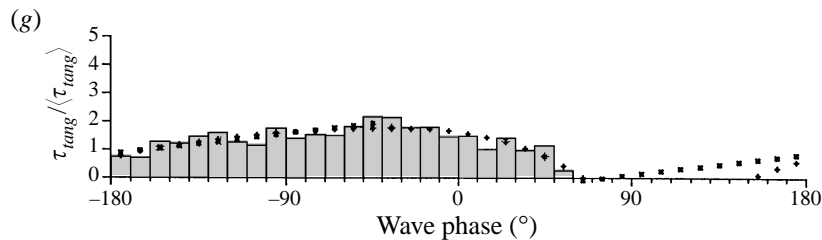
FIGURE 5(*e, f*). For caption see facing page.

(g)

FIGURE 5. Average waveforms with distributions as a function of wave phase of: surface velocity; tangential stress; 10° binned tangential stress; and, 10° binned wave coherent tangential stress. The smoothed 'inner' and 'outer' interpolated distributions of tangential stress used to derive the revised mean tangential stresses in table 1 are shown as $+$, $\times$, respectively, in the fourth panel in each case. The basis for these smoothed interpolations is shown in figure 5(g). (a) Wind speed 4.8 m s^{-1}, fetch 4.35 m. (b) Wind speed 6.3 m s^{-1}, fetch 2.45 m. (c) Wind speed 6.3 m s^{-1}, fetch 3.10 m. (d) Wind speed 6.3 m s^{-1}, fetch 4.35 m. (e) Wind speed 8.1 m s^{-1}, fetch 2.45 m. (f) Wind speed 8.1 m s^{-1}, fetch 4.35 m. (g) Smoothed interpolations of the normalized tangential stress shown in relation to the normalized tangential stress distribution for the ensemble of all data sets. $+$, $\times$ represent the 'inner' and 'outer' fits described in the text.

5. Results

Table 1 gives the details of the experimental conditions investigated here, including the fetches, wind characteristics and mean wave properties and breaking-wave passage rate. The primary results were the observed distributions along the wave profile. Mean values were then estimated from the data, as described below, and are also presented in table 1. Also included in this table are corresponding U_{10} estimates calculated by extrapolating U_{cl} to a 10 m height above mean sea level on the basis of a logarithmic layer profile using the observed u_* and z_0 values. We have given associated error estimates in the second column of the table. The error estimates for the mean tangential stress were based on the standard error of the mean.

5.1. *Distributions along the wave profile*

The distributions of tangential surface velocity, shear stress and related results along the representative wave profiles studied here are shown in figures 5(a)–5(f). In each of these composite figures, the uppermost panel shows the average wave surface profile, computed from an ensemble of over 1000 waves. A slight change in slope associated with the leading edge of the microscale breaking region is apparent just upwind of the mean water level in some of these profiles.

The second panel shows the individual data points in the surface velocity distribution from image-pairs used to observe the vertical shear. Two aspects of the velocity at the crest and downwind of the crest are noteworthy. First, there are relatively few points located at wave crests that have orbital velocities equal to the wave celerity. This does not imply that we sampled predominantly non-breaking waves or that the data was sampled below the linear sublayer. We examined a number of larger-scale PIV images of microscale breaking wave crests and observed that the particle velocities only begin to approach the wave celerity significantly ahead of the wave crest, at the rear of the roller region. Thus, the commonly held impression that the surface velocity in the wind drift layer continues to flow over a crest after it has broken is not consistent with our observations. On the contrary, the wake effect significantly reduces the linear sublayer current at the crest. This issue is taken up in detail in Peirson & Banner (1997). Secondly, there are a few points located downwind of the crest that also show velocities well below the wave celerity. Since our PIV technique was not able to measure the shear
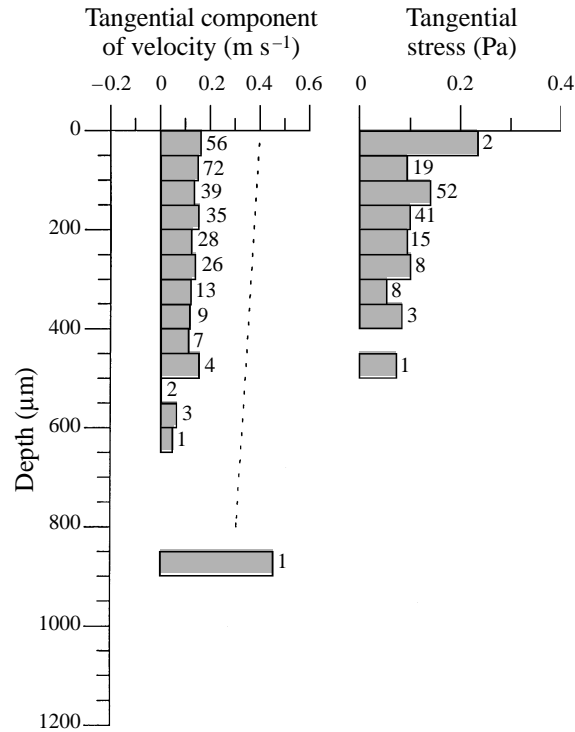
FIGURE 6. Distributions of velocity and tangential stress binned by distance from the interface. Fetch 4.35 m, wind speed 6.3 m s^{-1}. The slope of the dashed line indicates the expected rate of change of velocity away from the interface based on the mean measured tangential stress. The numbers to the right-hand side of each bar indicate the number of samples in each bin.

in the vicinity of spilling region, these points were the velocities associated with readable image-pairs used to measure the vertical shear and were only obtainable for non-breaking waves.

The third panel shows the distribution of the surface shear stress data points relative to the wave crest, based on about 140 measurements located within 1 mm of the interface. The fourth panel shows the same shear stress data binned over 10° of phase. No data is shown in the spilling regions, as PIV shear measurements were not possible in these regions. Highly scattered estimates were also obtained in the trough regions ahead of the spilling regions, where the local surface velocities were found to have low values, making it difficult to measure the surface shear, as seen in the surface velocity distributions. Also, the presence of transient patches of capillary waves introduced substantial variability associated with their locally strong vorticity levels (Longuet-Higgins 1992). The combination of these effects made it impossible to directly measure the local wind-induced shear stress in these regions and necessitated interpolating shear stress levels for these inaccessible regions in order to estimate mean tangential stress contributions. This aspect is discussed in §5.2.

The fifth panel shows the observed distribution of the wave-coherent shear stress $\langle \tau_{tang} u_{sw} \rangle / c$, in which the local wave-coherent tangential surface velocity u_{sw} was generated by subtracting the overall mean tangential velocity $\langle u_s \rangle$ from the measured tangential surface velocity distribution along the wave.

A further examination of the data consistency was performed to validate the assumption implicit in our analysis that the measurement was made within or in the
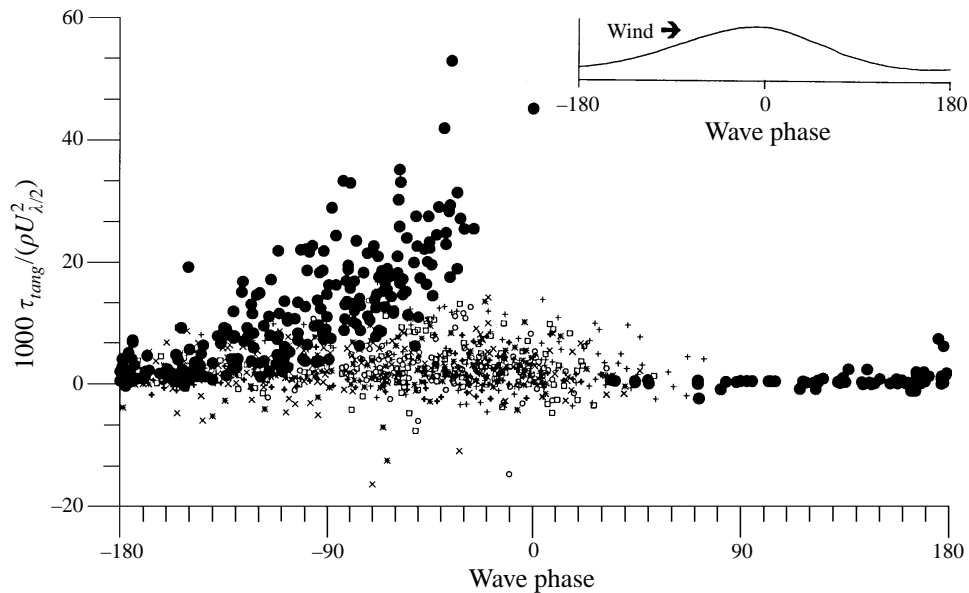
FIGURE 7. Estimates of surface tangential stress normalized by the wind speed half a wavelength above the mean water level from ●, Okuda *et al.* 1977 and this study: +, wind speed 4.8 m s⁻¹, fetch 4.35 m; ×, wind speed 6.3 m s⁻¹, fetch 2.45 m; ✳, wind speed 6.3 m s⁻¹, fetch 3.10 m; □, wind speed 6.3 m s⁻¹, fetch 4.35 m; ○, wind speed 8.1 m s⁻¹, fetch 2.45 m; +, wind speed 8.1 m s⁻¹, fetch 4.35 m.

immediate vicinity of the linear sublayer where the tangential stress can be estimated directly from the shear normal to the boundary. If a substantial proportion of the measurements were obtained outside the linear sublayer where the turbulent fluctuations carry a proportion of the total tangential stress, the net result would be an underestimate of the tangential stress. Figure 6 shows the distributions of mean velocity and tangential stress as a function of depth for a typical experiment at a given fetch and wind speed, irrespective of phase location along the wave profile. Indicated on the plot are the numbers of velocity or tangential stress estimates within a given 50 μm depth bin. Where there are adequate numbers of measurements, mean tangential velocities appear to decrease linearly with depth, and the tangential stress estimates do not appear to indicate any significant bias with depth. In fact, these data points all fall within a distance $0 < y^+ < 7$ of the interface, where $y^+ = yu_*/v$. These considerations confirm that our measurements have captured the behaviour of the linear sublayer.

For reference and discussion subsequently, a comparison of the present shear stress results with those obtained by O77 is shown in figure 7, in which the distribution of dimensionless shear stress is based on $U(\frac{1}{2}\lambda)$ as the normalizing velocity. This choice was made to best match wind-speed conditions in the two facilities. It is evident in this figure that the present results represent very significantly reduced shear stress levels compared with those reported by O77 for similar conditions.

5.2. *Mean results*

Mean values were derived by computing average values of the distributions at given phase points along the wave profile. However, as indicated above, no reliable data could be collected for some locations along the wave such as the spilling regions and trough regions. This necessitated estimating velocity and shear levels in these subregions to obtain the mean values that are shown in table 1. Three estimates of the
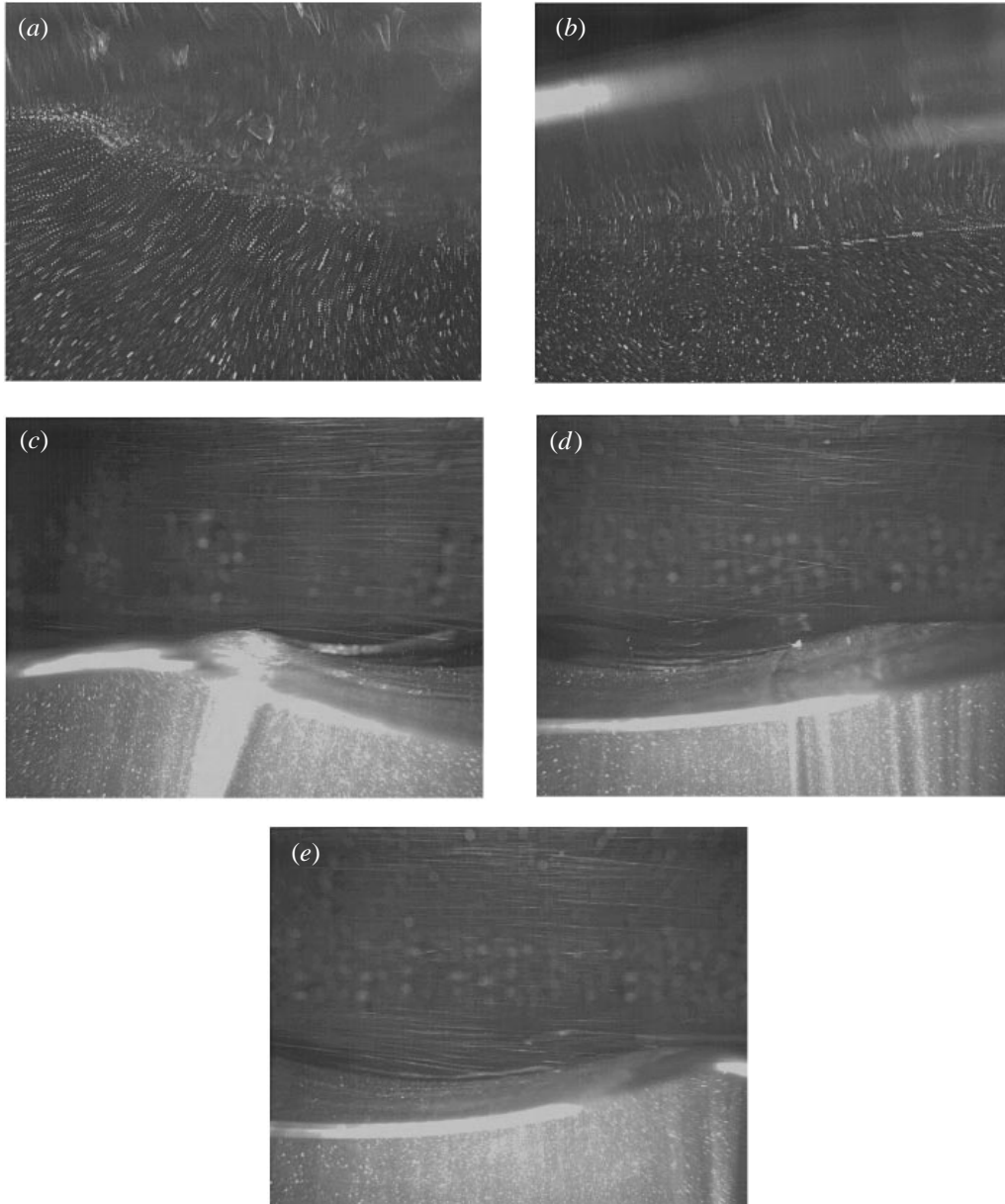
FIGURE 8. (*a*) and (*b*) show aqueous PIV images of the trough regions downwind of small-scale breaking wave crests at the 2.45 m fetch. The wind and waves are travelling from left to right, with the breaking crest on the left-hand side of the images. (*c*)–(*e*) show visualizations of water particles in the air flow above the wave surface, at the 4.35 m fetch. In the immediate foreground is the meniscus on the tank wall. The bright continuous line above this is the light-sheet interface with some near-surface particles visible. The bright streaks in the upper half of the pictures are water particles inejcted in the air flow. Droplets have been deposited on the tank wall creating bright spots in that region. (*a*) PIV image of trough region showing the lack of any organized viscous sublayer surface flow, confirming that this is a region of negligible tangential stress ($U_{cl} = 8.1$ m s^{-1}). (*b*) PIV image of trough region again showing the lack of any organized viscous sublayer surface flow. In addition, the flow re-attachment on the windward face is clearly visible through the organized viscous sublayer flow seen on the right-hand side of the image ($U_{cl} = 6.3$ m s^{-1}). (*c*) Airflow separation over a breaking crest ($U_{cl} = 8.1$ m s^{-1}). (*d*) Airflow reattachment in the vicinity of the downwind crest. The motion of a few water droplets is visible within the separation zone ($U_{cl} = 6.3$ m s^{-1}). (*e*) Airflow reattachment occurring just downwind of the trough ($U_{cl} = 6.3$ m s^{-1}).

mean surface current are shown. The first is simply the raw mean of the samples obtained from the experiments, with error estimates based on the standard error of the mean. A second estimate of the mean surface current was then made by assuming that this value is applicable along the windward face of the wave. In the spilling region, a value equal to the phase speed of the wave was assumed, together with a value of zero in the trough region. This procedure was justified on the basis of larger-scale aqueous PIV images of breaking crest and trough flow regions (e.g. see figure 8 a, b). These images confirmed visually that the spilling crests have particle speeds equal to the wave celerity, while the trough regions have almost zero horizontal velocity and negligible shear. In the region between the spilling zone and the trough, the weakly sheared forward drift velocity more or less offsets the rearward orbital motion. The mean values of the composite drift current have been compared with previous observations based on the empirical result $\bar{u}_s \sim 0.55u_*$, as reported by several authors based on timing buoyant particles, e.g. Phillips & Banner (1974). At our shortest fetch, the composite values given in table 1 compare very favourably with $0.55u_*$, but in the presence of waves, the composite surface drift current is less $0.55u_*$. The reasons for this difference are at present under investigation in an ongoing detailed study of the flow associated with microscale breakers.

Similarly, we calculated the sample mean tangential stresses and their associated standard error estimates. We then interpolated inferred tangential stress estimates in the measured tangential stress distributions where they could not be measured directly. These modified values are presented in the table as estimated mean tangential stress values. These were calculated by setting the tangential stress to zero at the toe of the spilling region (40°–70°) and in the separated airflow zone immediately downwind of it out to a phase angle of 160° (see figure 5). This physical picture was confirmed directly in our experiments by typical aqueous PIV images in trough regions, such as figures 8(a) and 8(b). For these strongly forced wind waves, these PIV images reveal negligible levels of vertical shear, and hence very weak tangential stress, in the region between the spilling zone and the trough. In addition, figure 8(b) also shows clearly the reattachment point just beyond the wave trough where the surface tangential stress has regenerated the wind drift sublayer flow at the commencement of the windward face of the downward wave.

During active breaking, the spilling region itself also experiences only weak tangential stress due to wind forcing, as it is embedded in a separated flow regime of the air flow. This was confirmed visually by water micro-droplet imagery in the air flow, such as shown in figure 8(c–e) and is consistent with the findings of Banner (1990). From these figures it is also apparent that the position of the downwind reattachment point can fluctuate substantially along the windward face of the waves during breaking.

In figure 5(a–f), it may be seen that a few isolated locations were undersampled at different phases within the ensemble of tangential stress distributions. In view of the physical and observational variability, we computed smoothed bounds for the observed tangential stress distributions along the wave profiles. These were based on assuming that the tangential stress distributions were self-similar to a first approximation, and were constructed by normalizing the tangential stress measurements obtained from each experiment by the corresponding estimated mean tangential stress values. These normalized values were accumulated for the entire data set and binned by wave phase to obtain the global normalized distribution of tangential stress, as shown in figure 5(g). Two smooth fits were then made to the normalized distribution of tangential stress to provide indicative error bounds for the estimated

mean tangential stress. Our 'outer' fit assumed a tangential stress variation that is approximately linear rearward from a phase of $-35°$ to a value of zero at $-200°$ (i.e. $70°$) and a best-fit quadratic curve between phases of $-35°$ and $70°$ (where the capacitance wave probe measurements determined the mean position of the toe or leading edge of the spilling region). This 'outer' fit provides an upper-bound estimate for extrapolation upwind of the trough where measurements were not possible. To provide a lower-bound estimate, an 'inner' fit was made using a best-fit quartic curve to the normalized distribution in figure 5(g), with mean tangential stress values of zero assigned between $70°$ and $160°$.

The two smoothed tangential stress profiles are shown in relation to the binned normalized data in figure 5(g). These profiles were then multiplied by the appropriate value of the estimated mean tangential stress for each case to obtain corresponding smoothed tangential stress distributions. These smoothed distributions are also shown superimposed in the fourth panel of each figure 5(a–f), for which it is seen that these provide satisfactory interpolation for each of the individual tangential stress data distributions. For each case, the two mean values derived from these interpolations were averaged to provide the revised tangential stress estimate shown in table 1. Their difference was typically $\pm 5\%$ and on this basis, the uncertainties associated with the smoothed fits to the tangential stress distribution were found to have only a minor effect on the estimated mean tangential stress levels.

5.3. *Tangential stress*

The behaviour of τ_{tang} with increasing fetch and for different wind speeds, shown in figure 9(a), indicates how the developing wave field influences the tangential stress. For each wind speed, the mean tangential stress tends to decrease slowly with fetch as the waves develop, except at the lowest wind speed, where it appears to increase slightly with fetch. It is remarkable that the tangential stress level for a given wind speed changes only modestly with wave development, despite the very high breaking intermittency and the strong changes in the appearance of the water surface roughness with increasing fetch evident in figure 2.

5.4. *Wind stress and relative contributions*

The wind stress was estimated from the friction velocity extracted from logarithmic layer regions of the mean velocity profiles in the air flow. This analysis also provided estimates for the aerodynamic roughness length z_0. The behaviour of τ with increasing fetch and for different wind speeds is shown in figure 9(b). The wind stress increases rapidly with fetch as the waves develop for each wind speed, implying that the wave-coherent stress soon becomes the dominant contributor to the wind stress.

Next, we examine how the relative contribution of the tangential stress to the total wind stress varies with the experimental conditions. Figure 10 shows various ways of presenting the trend of the data. Figure 10(a) plots the fraction τ_{tang}/τ as a function of the wave Reynolds number $U_{cl}\lambda/\nu$ for the various combinations of fetch and wind speed investigated in these experiments. This choice of non-dimensional parameter provides a reasonable collapse for this short-fetch data. With increasing wave Reynolds number, the asymptotic trend towards a fraction of $O(0.3)$ appears to be robust and is consistent with the observed fraction τ_{wave}/τ measured by Banner (1990) in the air flow. The use of u_* as an independent correlating variable for τ_{tang}/τ was less appropriate at short fetches/durations as τ_{tang} provides a significant proportion of the wind stress and hence of u_*. The behaviour with fetch is another possible way of
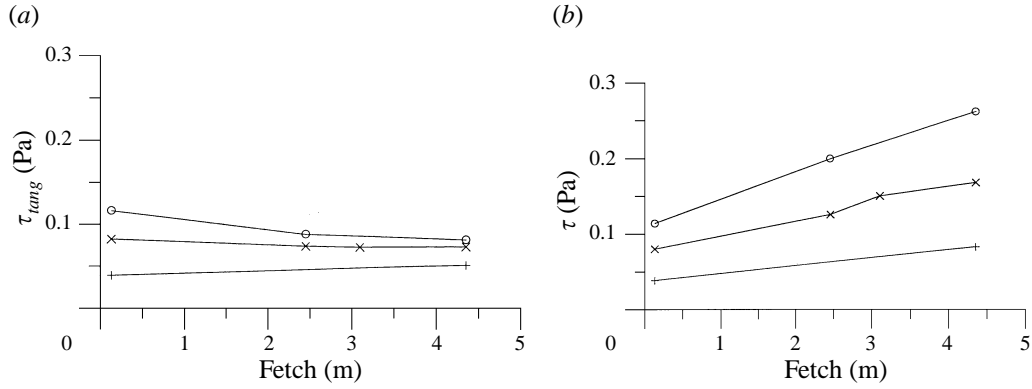
(*a*)

(*b*)

FIGURE 9. (*a*) Tangential stress versus fetch. Wind speeds: +, 4.8 m s^{-1}; ×, 6.3 m s^{-1}; ◯, 8.1 m s^{-1}. (*b*) Total stress versus fetch. Wind speeds: +, 4.8 m s^{-1}; ×, 6.3 m s^{-1}; ◯, 8.1 m s^{-1}.
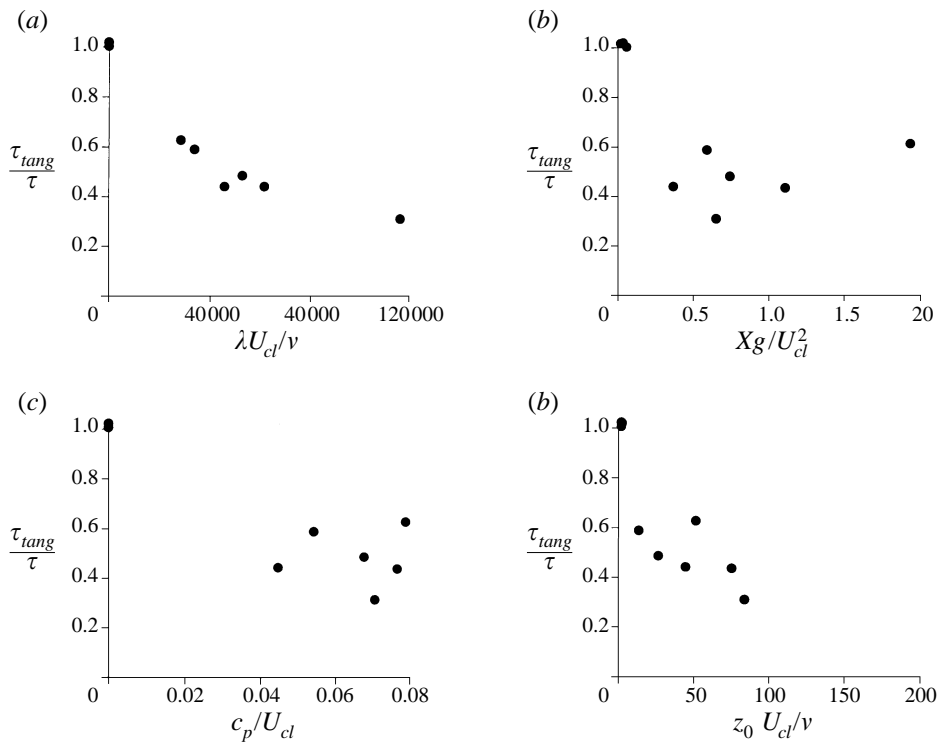
(*a*)

(*b*)

(*c*)

(*b*)

FIGURE 10. Stress ratio τ_{tang}/τ against (*a*) wave Reynolds number, (*b*) dimensionless fetch, (*c*) wave age, and (*d*) roughness Reynolds number based on U_{cl}.

correlating the data. Figure 10(*b*) shows the stress ratio as a function of the dimensionless fetch Xg/U_{cl}^2, but this does not provide a reasonable collapse of the data. Figure 10(*c*) presents another possible correlation, against wave age c_p/U_{cl}, where c_p is the phase speed of the dominant wave. It is evident that like the dimensionless fetch, this does not provide a systematic collapse of the data set. However, it is interesting to comment on the observed trend for τ_{tang}/τ towards about 0.3 seen in figure 10(*a*), which also results when this ratio is plotted against the roughness Reynolds number
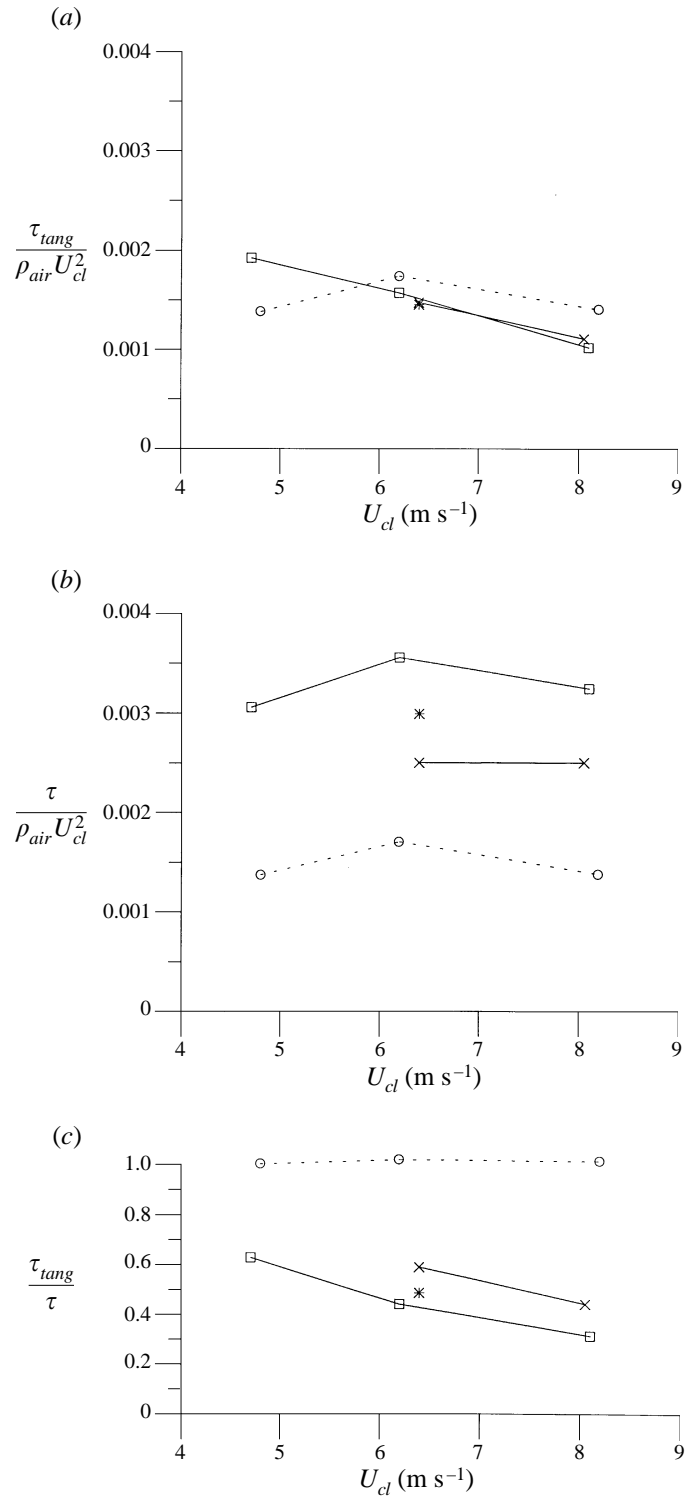
(*a*)

(*b*)

(*c*)

FIGURE 11. (*a*) Tangential drag coefficient against U_{cl}. Fetches: $\bigcirc$, 0.13 m; $\times$, 2.45 m; ✳, 3.10 m; $\square$, 4.35 m. (*b*) Total drag coefficient against U_{cl}. Fetches: $\bigcirc$, 0.13 m; $\times$, 2.45 m; ✳, 3.10 m; $\square$, 4.35 m. (*c*) Stress ratio τ_{tang}/τ against U_{cl}. Fetches: $\bigcirc$, 0.13 m; $\times$, 2.45 m; ✳, 3.10 m; $\square$, 4.35 m.

based on U_{cl} given by $R_{r,cl} = U_{cl} z_0 / \nu$, as seen in figure 10(*d*). This level might appear to be high at first sight, especially in light of the popular view that the sea surface does become fully aerodynamically rough. However, it should be mentioned that analogous results of Buckles, Hanratty and Adrian (1984) for the case of wind over comparably steep solid waves reported $\tau_{tang}/\tau \sim 0.11$, still indicative of transitionally rough rather than fully rough behaviour. The present results motivate a re-examination of the nature of the air flow over wind waves and its relation to the roughness Reynolds number, which is considered in §6.

To further investigate the dependence of the tangential stress on the wind forcing, a tangential drag coefficient $C_{t,cl} = \tau_{tang} / \rho_a U_{cl}^2$ based on the centreline wind speed is presented in figure 11(*a*) as a function of the centreline wind speed U_{cl}. The entire data set shows an overall decreasing trend for $C_{t,cl}$ with increasing centreline wind speed, except for the case of the lowest wind speed (4.8 m s^{-1}) at the shortest fetch. The denominator appears to be responsible for this departure from the general trend, as the tangential drag measurements in the numerator were repeatable to better than 10% at both 4.8 m s^{-1} and 6.2 m s^{-1} centreline wind speeds. Given that this trend was not apparent when plotted against extrapolated U_{10} velocities (see figure 12*a*), we decided not to pursue this further here.

For reference, the total drag coefficient $C_{d,cl} = \tau / \rho_a U_{cl}^2$ based on the centreline velocity is shown in figure 11(*b*). For the observed range of fetches, this figure shows a very strong fetch dependence, or rather, sea-state dependence, at any given wind speed. Clearly, with $C_{t,cl}$ relatively insensitive to the fetch, the strong fetch sensitivity in $C_{d,cl}$ arises from an increasing waveform drag contribution as the waves develop downwind.

Finally, the data in figures 11(*a*) and 11(*b*) can be combined to yield the behaviour of the stress ratio τ_{tang}/τ for the wave tank conditions. This is plotted in figure 11(*c*) and shows a decreasing trend for τ_{tang}/τ with wind speed, reaching a level of around 0.3 for the longest fetch studied. Again, once the waves have been initiated, there is no strong sea-state influence evident in the wind-speed trend of the data.

5.5. *Wave-coherent tangential stress and waveform drag*

With the assumption that the wave-coherent fluid velocity u_{sw} at the surface is given by subtracting the mean surface velocity $\langle u_s \rangle$ from the locally measured velocity u_s, the present data set allows an estimation of the wave-coherent tangential stress $\langle \tau_{tang} u_{sw} \rangle / c$. These estimates appear in table 1 and indicate that this contribution to the wave-coherent stress is a small fraction ($O(\frac{1}{20})$) of the overall wind stress.

The other wave-coherent stress contribution is the waveform drag. This is the momentum flux from the wind to the waves resulting from normal stress coherent with the wave slope. This quantity was not measured here, but may be estimated from the present data set. Invoking the familiar assumption that tangential stress is in local equilibrium across the fluid interface, the waveform drag is the difference between the wind stress and the tangential stress. While the tangential stress is continuous across the interface, the entire wind stress is not transmitted to the water side as there is a small net radiation of wave momentum flux that does not appear on the water side, unless the wave field is fully developed (see Donelan (1979)). The relative importance of the wave-coherent tangential stress contribution to the wave drag may be assessed from table 1, from which the wave form drag is estimated here as the difference between the observed wind stress and mean tangential stress. From this comparison, the wave-coherent tangential stress (second last row) is only an average of about 15% of the estimated form drag. We note that these form drag estimates are consistent with levels
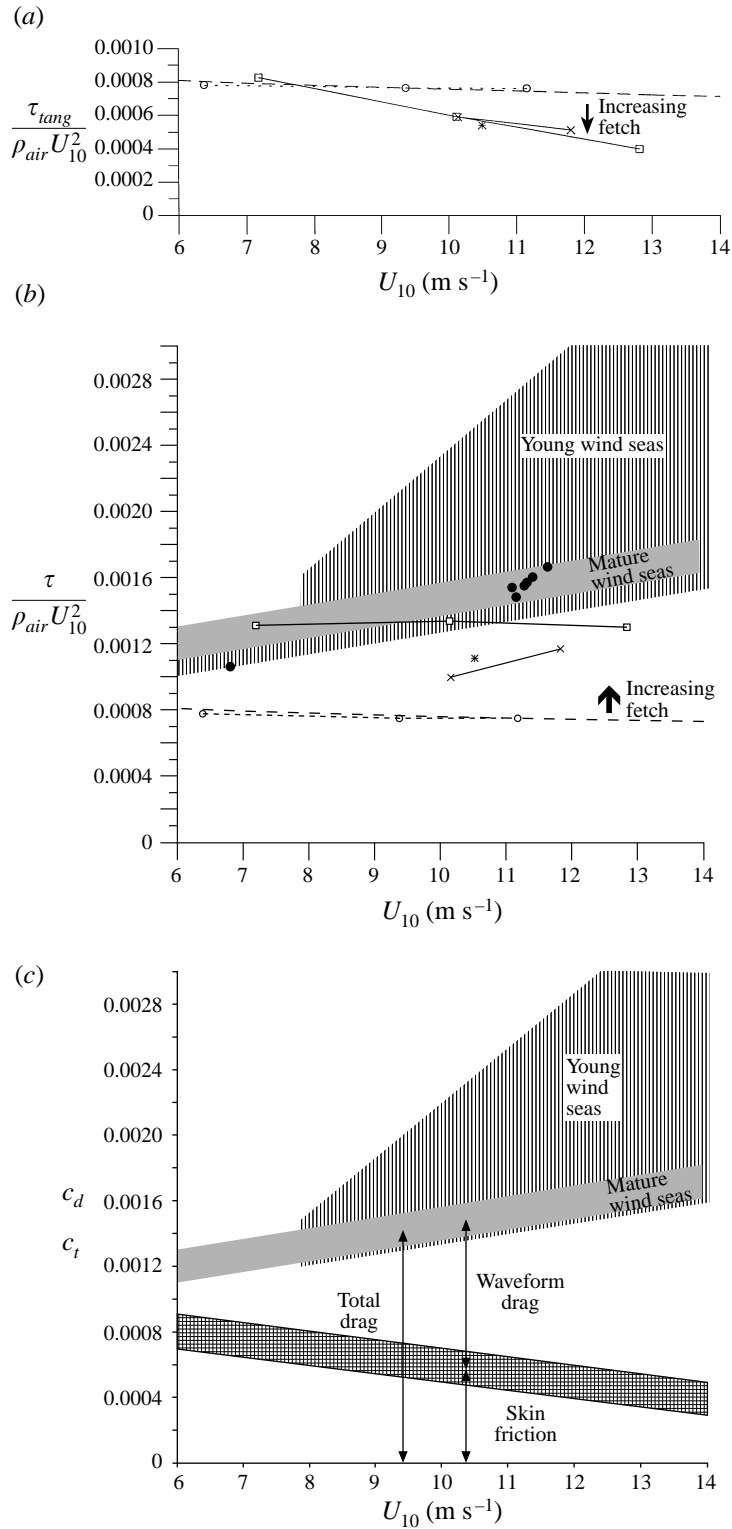
(a)

(b)

(c)

FIGURE 12. (a) Tangential drag coefficient versus U_{10}. Fetches: $\bigcirc$, 0.13 m; $\times$, 2.45 m; ✸, 3.10 m; $\square$, 4.35 m. The corresponding curve for turbulent flow over smooth walls is indicated by the dashed

implied by normal stress wave drag measurements reported in previous studies over similar very young wind waves (Banner 1990). This aspect is amplified in the discussion below.

6. Discussion

We believe that the measurements reported here resolve the prevailing disagreement on the relative importance of normal and tangential stress. On the one hand, the water side results of O77 led those authors to propose that for strongly forced laboratory wind-wave conditions, tangential surface stress dominates the wind stress. As pointed out earlier, this conclsuion is in conflict with the aerodynamic form drag measurements of Banner (1990), among others, whose results indicated that for strongly forced wind waves, wave form drag calculated by the correlation of normal stress with the wave slope provides the dominant contribution to the wind stress. The tangential stress levels on the water side determined by the present PIV methodology are significantly lower than those reported by O77, and are in close agreement with the difference between the wind stress and wind measurements of wave form drag. This provides a close correspondence between air side and water side tangential stress levels, consistent with the expected stress balance across the interface.

Before moving to a discussion of the implications for open ocean conditions, it is noted that before the onset of the wind waves, the water side tangential stress largely balances the entire wind stress. However, the instability of the wind drift current rapidly leads to the appearance of short, strongly forced wind waves that are in a state of microscale breaking, as is clear from the surface photographs shown in figure 2. As the wave field is established, the wave drag increases and, to a reasonable approximation, adds to the tangential stress to augment the wind stress. At what stage of wave development does the wave form drag match the tangential stress level? According to the present measurements (table 1), this was found to occur at relatively low roughness Reynolds number $R_r = u_* z_0/\nu$ levels of around 2. For higher R_r, the present measurements contribute new insight towards the debate on whether the air flow over wind waves becomes aerodynamically rough, as discussed below.

It is well known from classical boundary-layer studies that fluids flowing over stationary solid boundaries may be classified as aerodynamically smooth, transitional or rough depending on the local R_r. At one extreme, for sufficiently low $R_r (\sim 0.1)$, the boundary roughness elements are much smaller than the viscous sublayer thickness. The flow is aerodynamically smooth and is characterized by a viscous sublayer flow in which the entire boundary stress is transmitted by tangential viscous shear stress. At the other extreme, the boundary roughness elements are much taller than the typical depth of the visous sublayer and the organized viscous sublayer disappears. The flow is then classified as aerodynamically rough, and the stress is considered to be fully supported by form drag over the roughness elements, and the roughness length is proportional to the physical roughness height. For intermediate situations, the flow is termed transitional. The air–sea interaction community has borrowed heavily from these solid boundary-layer concepts, yet after several decades of investigations of wind

line. (*b*) Total drag coefficient against U_{10}. Fetches: ○, 0.13 m; ×, 2.45 m; ✱, 3.10 m; □, 4.35 m. ●, laboratory data from Donelan (1990, figure 4). The corresponding curve for turbulent flow over smooth walls is indicated by the dashed line. The scatter of sea surface C_d values for mature and young wind seas is indicated by the labelled hatched areas. (*c*) Composite diagram of the findings in figures 12(*a*) and 12(*b*) showing the relative contributions of the skin friction and form drag to the overall sea surface drag coefficient as a function of wind speed.

drag over water surfaces, there does not appear to be a consensus on whether the sea surface is ever fully rough.

In laboratory experiments, Banner (1990) and Donelan (1990) confirmed that form drag makes a dominant contribution to the wind stress. However, in the absence of direct tangential stress measurements, it is fair to say that the uncertainties in making form drag and wind stress measurements immediately above the instantaneous water surface have impeded the definitive conclusion that the entire wind stress was made up of form drag.

The present measurements now confirm directly that for the wind speed range investigated, a significant level of tangential stress persists even when the interface is dominated by microscale breaking waves, and so the air flow over laboratory wind waves encountered here was never fully rough. The present measurements show directly that even under very strong wind forcing, a viscous sublayer flow reforms on the windward face of the wind waves, predominantly microscale breakers, and this leads to a fractional contribution $\tau_{tang}/\tau \sim O(0.3)$ for sufficiently high wave Reynolds numbers. This level is consistent with the form drag results reported by Banner (1990), but is about twice that reported over comparably steep solid waves. However, this difference is not surprising considering the fundamentally different nature of the boundary conditions with solid wavy surfaces as discussed by Banner & Melville (1976) and Gent & Taylor (1976), amongst others. The essential difference is due to the mobility of the interface with its non-zero tangential velocity. In a frame of reference travelling with the waveform, this is seen to stabilize the air flow to the onset of separation.

6.1. *Implications for open ocean conditions*

A strong motivation for conducting this research was to elucidate the character of the air flow over the wind-driven sea surface. The nature of the air flow over the sea has certain similarities to that over land, but there are some fundamental differences introduced by the different boundary condition at the air–sea interface. The question of whether the sea surface becomes fully aerodynamically rough is a classical question in the air–sea interaction literature and has an extensive history, for which Donelan (1990) gives a perspicacious review and provides extensive insight into the current status of this issue. We now revisit this fundamental and classical question in the light of the present findings.

Compared with laboratory wind waves, the component of the wind stress over the ocean owing to wave drag arises from a much broader bandwidth spectrum of wind waves, with different steepnesses, directionality and spatial intermittency than the tank waves. The gustiness of the wind is also different. In fact, it is an ongoing active topic of discussion as to the extent to which laboratory and ocean wind-wave systems actually involve precisely the same physics (see the discussion by Jones & Toba (1995) and Donelan *et al.* (1995)). Hence trying to extrapolate the laboratory data to the field on the basis of a non-dimensional grouping, such as wave age or dimensionless fetch, has proved to be controversial. With this cautionary note, we will nevertheless attempt to relate the present findings to the microscale breaking structures that have been documented as commonly occurring at sea.

A major conclusion of the present study is that for wind speeds typical of open ocean conditions under medium to strong wind forcing, the mean tangential stress level manages to persist at an appreciable level. This is very remarkable considering the severe aerodynamic and hydrodynamic disturbance caused by the presence of intense small-scale breaking wave activity. It is evident (see figure 1) that microscale breaking

structures are a common feature of the wind driven sea surface. We now propose that for the same level of near-surface wind speed, these field conditions are unlikely to be locally more disruptive to the tangential stress than the disturbances imposed by the present laboratory microscale breakers. If anything, for comparable wind speeds, field conditions appear to be, on average, less severe locally. For example, under open ocean conditions corresponding to $U_{10} = 12.8$ m s^{-1}, typical drag coefficient levels for mature wind seas are reported around 0.0016 (e.g. Wu 1980). This gives a friction velocity $u_* \sim 0.51$ m s^{-1} and a roughness length $z_0 \sim 0.19$ mm. Our short-fetch wave-tank measurements at the same extrapolated wind speed of $U_{10} = 12.8$ m s^{-1}, for which $U_{cl} = 8.1$ m s^{-1} at 4.35 m fetch, gave friction velocity and roughness length values of 0.47 m s^{-1} and 0.15 mm, respectively. While marginally lower than the indicative field values, their close correspondence implies a very comparable near-surface wind-speed level. Recall that for strongly forced laboratory waves, the observed tangential stress levels depended primarily on the wind speed, and for a given wind speed, they were insensitive to the sea state. This implies that similar surface tangential stress levels should exist for fully developed field situations and strongly forced laboratory waves for comparable U_{10} wind speeds. Since the total wind stress levels are also similar, the total wave drag contributions for our strongly forced laboratory waves and fully developed field situations must also be comparable at similar U_{10} wind speeds.

The immediate question then arises: how can the very narrow bandwidth wind-wave system in the laboratory contribute the same wave drag as a broad spectrum of ocean waves? The answer lies in the much higher mean momentum density (momentum per unit surface area) of the laboratory microscale breaking waves than their ocean counterparts. Waveform drag is the integrated spectral wave momentum density times a spectral growth rate, integrated over the wave spectrum. To a first approximation, if one uses the spectral growth rate correlation due to Plant (1982) as representative, the waveform drag is proportional to the product of the square of the friction velocity and the upwind/downwind slope spectrum of the waves. Typical upwind/downwind mean square slope (m.s.s.) levels for the laboratory waves at $U_{10} \sim 12.8$ m s^{-1} are around 0.05, while the comparable upwind/downwind m.s.s. contribution for the entire ocean wave spectrum for this wind speed is only about 0.04 (Cox & Munk 1954). This argument suggests that the microscale breaking-wave structures distributed over the sea surface are not as energetic on average as they are in the laboratory when they are the dominant waves, and accordingly contribute significantly less waveform drag at similar U_{10} wind speeds.

The lower mean m.s.s. contribution of the short gravity wind wavelets in the field indicates that on average, they create less disturbance to the tangential stress supported in the wind drift layer. The present experiments show that the mean tangential stress level persists at an appreciable fraction of the wave-free level in the presence of very strongly forced, small-scale breaking waves with a very high breaking fraction. From the discussion above, it appears unlikely that field conditions become more severe locally than this for a wide range of commonly encountered U_{10} wind-speed levels, except possibly at gale force winds and beyond, where the fluid mechanics of the interface may be modified by effects such as bursting bubbles and spray production.

Quantitatively, our wave-tank data have been extrapolated to field conditions by estimating U_{10} values corresponding to the observed u_*^a and z_0 values on the basis of the usual logarithmic mean velocity profile relationship $U_{10} = u_*/\kappa \ln(10/z_0)$, with $\kappa = 0.4$. When presented in this way, our very short-fetch data in figure 12(a) confirm that the wave-free (zero fetch) cases correspond very closely to the familiar drag coefficient relationship $C_{ds} = u_*^2/U_{10}^2$ for smooth wall turbulent boundary layers. This

curve was calculated by setting $z_0 = \nu/11u_*$ and solving iteratively for C_{ds} using the above logarithmic velocity profile relationship. This gives the slowly decreasing dependence with wind speed shown superimposed in figures 12(a) and 12(b).

Further downwind, the presence of active microscale breaking wavs as the dominant wind waves in the system produces a modest decline with wind speed in the extrapolated tangential drag coefficient $C_t = \tau_{tang}/\rho_a U_{10}^2$ from 8×10^{-4} at $U_{10} \sim 7$ m s^{-1} to 4×10^{-4} at $U_{10} \sim 13$ m s^{-1}. Importantly, this trend appears insensitive to the scale of the microscale breakers and mirrors the behaviour seen previously in figure 11(a). Now, if it is accepted that the near-continuous small-scale breaking found at very short fetches is representative of the most severe disruption to the viscous sublayer structure, then this curve is a plausible lower bound for the likely behaviour of C_t in the field. The upper bound for C_t is the smooth surface curve specified by C_{ds} as discussed above. On the basis of the present results, it is proposed that C_t in the open ocean falls between these two trend curves, but probably closer to the lower curve, for all wave age conditions.

The trend of C_t with wind speed now needs to be related to the corresponding trend of the familiar drag coefficient C_d for the total wind stress. The present laboratory results for C_d extrapolated to U_{10} are plotted in figure 12(b), which, for comparison, shows the wave-free smooth-surface data and theoretical smooth-wall form for C_d. It is seen that in the presence of developing microscale breakers, at a given wind speed the extrapolated C_d values increase strongly with increasing fetch, or equivalently, 'sea state'. In a longer wind-wave tank, higher C_d values have been reported at greater fetches (e.g. Donelan (1990), figure 4) and have been plotted on this figure. However, our observed C_d values did not show the familiar increase with wind speed. Also, again for comparison, the trend of field C_d data is included in figure 12(b). The pronounced difference between mature field waves ($U_{10}/c_p < 1$) and very young field waves ($U_{10}/c_p > 3$) taken from figure 4 in Donelan (1990) is also highlighted in this figure. Given the apparently strong sea-state dependence in C_d, and relatively weak sea-state dependence for C_t, considerable care must be taken in drawing conclusions about the relative importance of tangential and wave-drag contributions to the wind stress, and hence on the fundamental issue of sea-state roughness, as discussed below.

The present data implies that the air flow over the sea does not become fully aerodynamically rough, at least for wind speeds up to around 15 m s^{-1}. This conclusion follows from the findings reported here in relation to the field data C_d results plotted in figure 12(b). From that data, typical C_d levels for very young wind seas at $U_{10} \sim 13$ m s^{-1} reach 0.003, while for mature seas $C_d \sim 0.0016$. For the latter, subtracting the extrapolated tangential drag coefficient of 0.0004 leaves a waveform drag coefficient of 0.0012, implying that $\tau_{tang}/\tau_w \sim 0.33$. Even for very young ocean waves, the aerodynamically roughest conditions, a similar calculation gives $\tau_{tang}/\tau_w \sim 0.16$, indicating that even during these strong transient wind-forcing events, the air flow is still not fully aerodynamically rough. A visual summary of the implications of the field extrapolations in figures 12(a) and 12(b) is shown in figure 12(c). These considerations largely confirm the discussion at the end of §4.10 in Phillips (1977), where it is concluded that the air flow over the sea surface is better described as transitionally rough.

Finally, it is noted that the present results are in conflict with the Kitaigorodskii (1968) argument that $z_0 \sim \sigma$ (the r.m.s. wave height) implies fully rough behaviour by analogy with the rough-wall case. Even though our data shown in figure 13 conform to this trend, in agreement with previous studies, it has been established directly in this study that tangential stress is non-negligible even for our roughest conditions. The
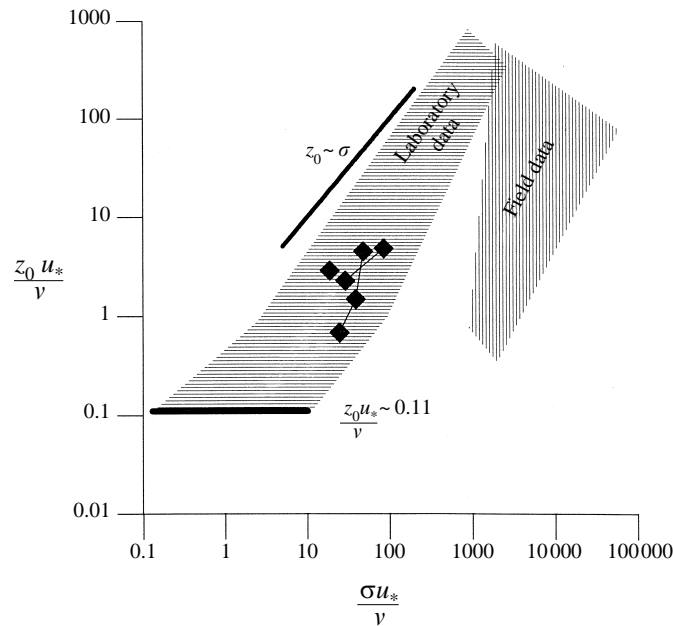
FIGURE 13. The results of this study superimposed on figure 11 of Donelan (1990), showing the roughness Reynolds number $z_0 u_*/\nu$ plotted against the normalized r.m.s. wave height $\sigma u_*/\nu$. ◆, present results. The scatter of laboratory and open ocean data from previous studies is indicated by the labelled hatched areas. Note that the present wave-free very short fetch data is not shown and lies well to the left of the ordinate axis close to the indicated smooth-wall asymptote.

interested reader is referred to §4 in Donelan (1990), for additional discussion on this issue.

Refining these estimates remains a challenge owing to our present incomplete understanding of how to properly calculate or measure the form drag contribution for open ocean conditions, especially if the form drag contributions from both non-breaking and breaking waves are taken into account. However, in a recent paper modelling the atmospheric drag over the sea surface, Makin, Kudryavtsev & Mastenbroek (1995) predict τ_w/τ values somewhat higher than implied by the present findings. At $U_{10} = 13$ m s^{-1} for mature wind seas, they predict $\tau_w/\tau \sim 0.85$ or $\tau_{tang}/\tau_w \sim 0.18$, whereas our observations suggest $\tau_w/\tau \sim 0.77$ or $\tau_{tang}/\tau_w \sim 0.3$. At higher wind speeds, into the gale force range, Makin *et al.* (1995) predict an increasingly higher contribution to the wind stress from form drag, but the local physics of the sea surface may well change owing to local surface detachment and spray formation, thereby producing a different interfacial flow regime and stress balance. Examination of such conditions is beyond the scope of the present study.

7. Conclusions

In our wind-wave tank, we have measured representative shear stress levels in the aqueous viscous sublayer immediately below strongly wind-forced, short gravity waves that were characterized by frequent microscale breaking. We also obtained complementary properties of the wind stress based on the logarithmic mean velocity profile technique. The results obtained in this study provide the following conclusions:

(i) Our very short-fetch measurements have shown that tangential stress in the surface layer immediately beneath a wind-driven interface in the absence of any

background wind waves contributes the entire interfacial stress. However, at longer fetches following the inception of wind waves, the tangential stress in the aqueous viscous sublayer does not account for the entire wind stress. This is contrary to the findings of O77 that the tangential stress associated with very short wind waves supports the entire wind stress. The present PIV methodology overcomes the significant experimental errors inherent in their hydrogen bubble methodology.

(ii) The relative contribution that tangential stress makes to the overall wind stress depends on the stage of development of the wind waves. Before the onset of wind waves, the wind stress is entirely supported by tangential stress. As the wave field develops, the waveform drag component becomes increasingly important and soon provides the dominant contribution. The extent to which waveform drag dominates the tangential drag depends on the sea state, but this cannot yet be quantified precisely because of our present incomplete knowledge of how to calculate the wave drag.

(iii) Our measurements show that there was a modulated tangential stress component in phase with the wave elevation. However, the asssociated wave-coherent shear stress levels were estimated here as typically only a small [$O(0.05)$] fraction of the total wind stress, indicating that form drag dominates the wave-coherent momentum flux. This is consistent with conclusion (ii) above.

(iv) Our short-fetch tangential stress measurements reveal that the tangential stress levels have only a relatively weak dependence on the wave conditions for a given wind speed. On this basis, physical arguments are advanced for extrapolating the present findings to the field. It is proposed that for a given wind speed, the mean tangential stress contribution to the wind stress is insensitive to the sea state conditions, and decreases slowly with increasing wind speed. The tangential stress contribution to the wind stress, while subordinate to the wave drag contribution at windspeeds above 9 m s^{-1}, is still likely to remain significant for wind speeds of 15 m s^{-1}, and possibly for even higher wind speeds.

Typically, our results indicate that for mature wind seas, the tangential stress contributes a significant but decreasing fraction of the total wind stress as the wind speed increases. For transient, very young wind seas, this fraction is reduced but is still not negligible. Thus, for the moderate-to-strong wind speed regime of $U_{10} \sim 6 \text{ m s}^{-1}$ to 15 m s^{-1}, and over a wide range of sea states, the air flow is best characterized as transitionally rough.

REFERENCES

BANNER, M. L. 1990 The influence of wave breaking on the surface pressure distribution in wind–wave interactions. *J. Fluid. Mech.* **211**, 463–495.

BANNER, M. L. & MELVILLE, W. K. 1976. On the separation of air flow over water waves. *J. Fluid. Mech.* **77**, 825–842.

BUCKLES, J., HANRATTY, T. J. & ADRIAN, R. J. 1984 Turbulent flow over large amplitude wavy surfaces. *J. Fluid. Mech.* **140**, 27–44.

COKELET, E. D. 1977 Steep gravity waves in water of arbitrary uniform depth. *Phil. Trans. R. Soc.* A **286**, 183–230.

COX, C. S. & MUNK, W. 1954 Statistics of the sea surface derived from sun glitter. *J. Mar. Res.* **13**, 198–227.

CSANADY, G. T. 1985 Air–sea momentum transfer by means of short crested wavelets. *J. Phys. Oceanogr.* **15**, 1486–1501.

CSANADY, G. T. 1990 Momentum flux in breaking wavelets. *J. Geophys. Res.* **95**, 13 289–13 299.

DONELAN, M. A. 1979 On the fraction of wind momentum retained by waves. In *Marine Forecasting, Predictability and Modelling in Ocean Hydrodynamics* (ed. J. C. Nihoul). Elsevier.

DONELAN, M. A. 1990 Air–sea interaction. In *The Sea: Ocean Engineering Science*, pp. 239–292. Wiley.

DONELAN, M. A., DOBSON, F. W., SMITH, S. D. & ANDERSON, R. J. 1995 Reply to 'Comments on The dependence of sea surface roughness on wave development'. *J. Phys. Oceanogr.* **25**, 1908–1909.

GENT, P. & TAYLOR, P. A. 1976 A numerical model of air flow above water waves. *J. Fluid Mech.* **77**, 105–128.

JEFFREYS, H. 1924 On the formation of waves by wind. *Proc. R. Soc. Lond.* A **107**, 189–206.

JEFFREYS, H. 1925 On the formation of waves by wind. II. *Proc. R. Soc. Lond.* A **110**, 341–347.

JONES, I. S. F. & TOBA, Y. 1995 Comments on 'The dependence of sea surface roughness on wave development'. *J. Phys. Oceanogr.* **25**, 1908–1909.

KITAIGORODSKII, S. A. 1968 On the calculation of the aerodynamic roughness of the sea surface. *Dokl. Akad. Nauk SSSR. Atmos. Oceanic Phys.* **4**, 870–878.

KLINE, S. J., REYNOLDS, W. C., STRAUB, F. A. & RUNSTADLER, P. W. 1967 The structure of turbulent boundary layers. *J. Fluid Mech.* **30**, 741–773.

LONGUET-HIGGINS, M. S. 1992 Capillary rollers and bores. *J. Fluid Mech.* **240**, 659–679.

McLEISH, W. & PUTLAND, G. E. 1975 Measurements of wind-driven flow profiles in the top millimeter of water. *J. Phys. Oceanogr.* **5**, 516–518.

MAKIN, V. K., KUDRYAVTSEV, V. N. & MASTENBROEK, C. 1995 Drag of the sea surface. *Boundary-Layer Met.* **73**, 159–182.

PEIRSON, W. L. 1997 Measurement of surface velocities and shears at a wavy air–water interface using particle image velocimetry. *Exps. Fluids* **23**, 427–437.

PEIRSON, W. L. & BANNER, M. L. 1997 On the surface kinematics of microscale breaking waves. In preparation.

PHILLIPS, O. M. 1977 *The Dynamics of the Upper Ocean*. Cambridge University Press, 336 pp.

PHILLIPS, O. M. & BANNER, M. L. 1974 Wave breaking in the presence of wind drift and swell. *J. Fluid. Mech.* **66**, 625–640.

PLANT, W. J. 1982 A relationship between wind stress and wave slope. *J. Geophys. Res.* **87**, 1961–1967.

OKUDA, K., KAWAI, S. & TOBA, Y. 1977 Measurement of skin friction distribution along the surface of wind waves. *J. Oceanogr. Soc. Japan* **30**, 190–198.

WILKINSON, D. L. & WILLOUGHBY, M. A. 1981 Velocity measurements with hydrogen bubbles – the wake effect. *J. Hydraulic Res.* **19**, 141–153.

WU, J. 1980 Wind stress coefficients over the sea surface near neutral conditions – a revisit. *J. Phys. Oceanogr.* **10**, 727–740.